KeA1

CHINESE ROOTS
GLOBAL IMPACT

#### Contents lists available at ScienceDirect

# Petroleum Science

journal homepage: www.keaipublishing.com/en/journals/petroleum-science



# Original Paper

# Simulation study of supercritical carbon dioxide jet fracturing for carbonate geothermal reservoir based on fluid-thermo-mechanical coupling model



Jian-Xiang Chen <sup>a</sup>, Rui-Yue Yang <sup>a, \*</sup>, Zhong-Wei Huang <sup>a</sup>, Xiao-Guang Wu <sup>a</sup>, Shi-Kun Zhang <sup>b</sup>, Hai-Zhu Wang <sup>a</sup>, Feng Ma <sup>c, d</sup>

- <sup>a</sup> State Key Laboratory of Petroleum Resources and Prospecting, China University of Petroleum, Beijing, 102249, China
- <sup>b</sup> Sinopec Research Institute of Petroleum Engineering, Beijing, 102206, China
- <sup>c</sup> The Institute of Hydrogeology and Environmental Geology, Chinese Academy of Geological Sciences, Shijiazhuang, 050061, Hebei, China
- <sup>d</sup> Technology Innovation Center of Geothermal & Hot Dry Rock Exploration and Development, Ministry of Natural Resources, Shijiazhuang, 050061, Hebei, China

#### ARTICLE INFO

# Article history: Received 1 April 2022 Received in revised form 1 November 2022 Accepted 2 November 2022 Available online 5 November 2022

Edited by Yan-Hua Sun

Keywords:
Carbonate
Carbon capture utilization and storage
(CCUS)
Jet fracturing
Coupled model
Geothermal reservoir

#### ABSTRACT

Geothermal energy is a kind of renewable, sustainable and clean energy resource. Geothermal energy is abundant in carbonate reservoirs. However, low matrix permeability limits its exploitation. The supercritical carbon dioxide (SC–CO<sub>2</sub>) jet fracturing is expected to efficiently stimulate the carbonate geothermal reservoirs and achieve the storage of CO<sub>2</sub> simultaneously. In this paper, we established a transient seepage and fluid-thermo-mechanical coupled model to analyze the impact performance of SC-CO<sub>2</sub> jet fracturing. The mesh-based parallel code coupling interface was employed to couple the fluid and solid domains by exchanging the data through the mesh interface. The physical properties change of SC-CO<sub>2</sub> with temperature were considered in the numerical model. Results showed that SC-CO<sub>2</sub> jet fracturing is superior to water-jet fracturing with respect to jetting velocity, particle trajectory and penerability. Besides, stress distribution on the carbonate rock showed that the tensile and shear failure would more easily occur by SC-CO<sub>2</sub> jet than that by water jet. Moreover, pressure and temperature control the jet field and seepage field of SC-CO<sub>2</sub> simultaneously. Increasing the jet temperature can effectively enhance the impingement effect and seepage process by decreasing the viscosity and density of SC-CO<sub>2</sub>. The key findings are expected to provide a theoretical basis and design reference for applying SC-CO<sub>2</sub> jet fracturing in carbonate geothermal reservoirs.

© 2022 The Authors, Publishing services by Elsevier B.V. on behalf of KeAi Communications Co. Ltd. This is an open access article under the CC BY-NC-ND license (http://creativecommons.org/licenses/by-nc-nd/4.0/).

# 1. Introduction

With traditional fossil energy exhausted and climate change catastrophic effects, the need for renewable energy is more and more urgent. The carbonate geothermal reservoir is an excellent alternative energy source due to its high thermal conductivity and wide distribution (Wang et al., 2021). However, the hydraulic conductivity of the carbonate formations is mainly controlled by tectonic structures and karstification (Homuth et al., 2015). That means the permeability of the carbonate reservoir is highly related to the primary fracture networks. The field tests showed the matrix

perforation, hydraulic fracturing and hydraulic isolation. This technology is widely used in the oil and gas industry to create fracture networks and increase reservoir permeability (Li et al., 2010; Sheng et al., 2013).

SC-CO<sub>2</sub> fluid is a special supercritical fluid with a density similar

permeability was very low  $(10^{-16}-10^{-15} \text{ m}^2)$ , even for the core

samples with the highest porosity (Niederau et al., 2015). The low matrix permeability limits the exploitation of carbonate

geothermal reservoirs. Therefore, stimulation treatments are

necessary for the target strata with poorly developed fracture

networks to efficiently develop geothermal resources. Hydraulic jet

fracturing is a method that integrates the operations of jetting

SC-CO<sub>2</sub> fluid is a special supercritical fluid with a density similar to an ordinary liquid and a viscosity similar to gas. It is generated when the temperature and pressure are above its critical values

<sup>\*</sup> Corresponding author.

E-mail address: yangruiyue@cup.edu.cn (R.-Y. Yang).

 $(T_c=31.1\,^{\circ}\text{C}$  and  $P_c=7.38\,\text{MPa})$  (Sodeifian et al., 2019a, 2021). Benefit by the advantages of no residue, non-toxicity, recyclability, environmentally friendly, and availability at low cost, supercritical carbon dioxide (SC–CO<sub>2</sub>) is widely used in industrial field, such as oil extraction, solubility of the drug, separation of nanoparticles and chemical reaction (Sodeifian et al., 2016a, 2016b, 2017, 2019b, 2020a). In petroleum engineering, supercritical CO<sub>2</sub> (SC–CO<sub>2</sub>) has been introduced into fracturing due to its high diffusion coefficient and low surface tension. What's more, the SC–CO<sub>2</sub> could help extract oil and dissolved organic in the porosity (Ameri et al., 2020; Ardestani et al., 2020; Razmimanesh et al., 2021; Sodeifian et al., 2020b).

In carbonate geothermal reservoir conditions, CO<sub>2</sub> can reach its supercritical state easily. Furthermore, the interactions of CO<sub>2</sub>water-rock can induce dolomite dissolution in carbonate geothermal reservoirs. This could help to further increase the porosity and permeability. In the geothermal production stage, the dissolution reaction of dolomite and clay minerals can overshadow the precipitation effect of calcite and increase the heat mining rate (Cui et al., 2017). Due to the dissolution mechanism, a large quantity of CO<sub>2</sub> will be permanently sequestrated in the formation after the geothermal exploitation (Cui et al., 2016). Attributed to the excellent properties mentioned before, CO2 is selected as the fracturing fluid of jet fracturing to stimulate the geothermal reservoirs in this paper (Fig. 1). The SC-CO<sub>2</sub> jet fracturing generally contains two steps, jetting perforation and jet pressurization. First, the abrasive SC-CO<sub>2</sub> jet creates the jet hole and then the fracturing procedure is accomplished under the jet pressurization effect. In this paper, we mainly focused on the first step to analyze the flow field and impact stress of the SC-CO<sub>2</sub> jet. Applying SC-CO<sub>2</sub> jet fracturing in carbonate geothermal reservoirs is a complex process. It contains compressible fluid flow, particle migration, and fluid-thermo-mechanical coupling impingement. Therefore, a comprehensive study is needed to clarify the flow field, erosion pattern of particles, and the failure scheme of rock under SC-CO<sub>2</sub> jet impingement.

In previous studies, Wang et al. (2015) investigated the properties of the SC-CO<sub>2</sub> jet through the computational fluid dynamics method. They found that the compressibility of the SC-CO<sub>2</sub> jet could cause an extra intense impinging load for the perforation. Besides, results also demonstrated that the flow field of the SC-CO<sub>2</sub> jet is similar to that of the water jet. However, others found that temperature and heat transfer distributions in the jet-hole differ from the water jet, which has a noticeable effect on fracture initiation and propagation (Cai et al., 2017). Cai et al. (2020) investigated the

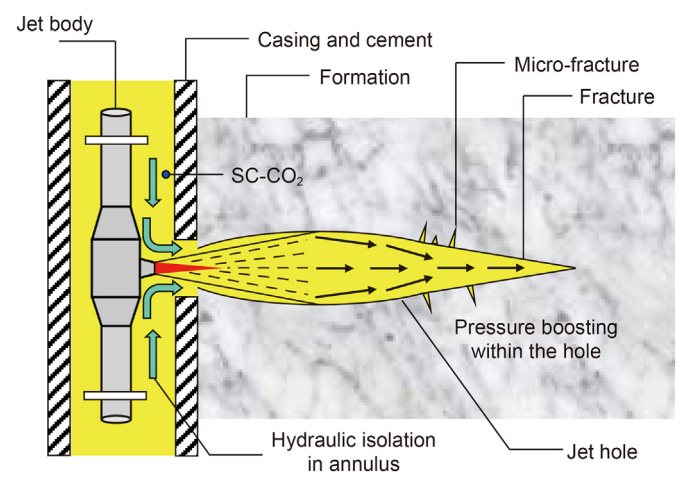


Fig. 1. The schematic diagram of SC-CO<sub>2</sub> jet fracturing.

SC-CO<sub>2</sub> jet flow field and induced strain response in the rock via high-speed photography. In addition, Cai et al. (2018) also deeply analyzed the influence of pressure drop, standoff distance, and nozzle diameter on the SC-CO<sub>2</sub> jet fracturing. In the jet hole, the jet pressurization effect needs to be considered. The pressurization of the SC-CO<sub>2</sub> jet in the jet hole leads to fracture initiation and propagation (Cai et al., 2018, 2022).

Furthermore, Hu et al. (2017) conducted experiments to explore the influence of pressurization on fracture initiation and propagation. He et al. (2015) studied the pressurization mechanism of SC-CO<sub>2</sub> jet in perforation and investigated the influences of pressure difference, ambient pressure, nozzle diameter, and fluid temperature by experiments. Other research also shows that the SC-CO<sub>2</sub> jet fracturing performs better on pressurization than water jet, generating fractures and propagating cracks at a lower pressure (Cai et al., 2018). And the lower initiation and propagation pressure are mainly attributed to the different temperatures and heat transfer of SC-CO<sub>2</sub> in the jet-hole (Hu et al., 2016). Besides, the thermo-elastic stresses induced by CO<sub>2</sub> phase change within cracks can create branching and crossing fractures around the main crack, forming the fracture networks (Huang et al., 2018).

Previous studies have analyzed the flow field of the SC-CO<sub>2</sub> jet and the pressurization mechanism in the jet hole based on numerical simulations and experiments. However, during perforation, the influence of jet temperature, pressure drop and phase change of SC-CO<sub>2</sub> on the evolution of transient impacted stress were still unclear. In addition, the seepage characteristic of SC-CO<sub>2</sub> in high-temperature carbonate rock pores is rarely studied during the jet fracturing process.

In this paper, a transient SC-CO<sub>2</sub> jet fracturing model was established to analyze the impact performance of jet fracturing. We adopted the RNG k- $\epsilon$  model to simulate the flow field of the SC-CO<sub>2</sub> jet. And the model was validated with the previously published experimental data. The cause of the difference in fracture propagation between SC-CO<sub>2</sub> and water jet was determined by analyzing the erosion rate of abrasive particles. Then, we employed the fluid-thermo-mechanical coupling model based on MpCCI to investigate the impact stress and thermal stress distribution. Finally, the seepage flow field of jet fracturing was studied. This work provided a better understanding of the application of the SC-CO<sub>2</sub> jet fracturing in carbonate geothermal reservoirs.

#### 2. Mathematical model

#### 2.1. The state equations of SC-CO<sub>2</sub>

As a compressible fluid, the density, viscosity, and thermal coefficient of SC-CO<sub>2</sub> vary significantly with temperature and pressure (Wu et al., 2022). In our jet fracturing model, the SC-CO<sub>2</sub> forms into a high-speed jet under high pressure and high temperature, which will significantly change the physical properties of SC-CO<sub>2</sub>. The state equations of CO<sub>2</sub> modified by the Span and Wagner (1996) via several experiments are commonly used by scholars. Their equations introduce dimensionless Helmholtz free energy to calculate the state parameters (Span, 2013). That makes the equations suitable for calculating the density and thermal conductivity under a wide range of pressure and temperature, from the triplepoint temperature to 1100 K and pressure up to 800 MPa, respectively. The dimensionless expression is (Span and Wagner, 1996):

$$\Phi(\delta,\tau) = \Phi_{0}(\delta,\tau) + \Phi_{r}(\delta,\tau) \tag{1}$$

Based on the Span-Wagner equations, the parameters of compressibility factor Z, the specific heat capacity at constant pressure  $C_D$ , and the Joule-Thomson coefficient  $C_I$  are calculated as

below (Span and Wagner, 1996):

$$Z = \frac{\rho(\delta, \tau)}{\rho RT} = 1 + \delta \frac{\partial \Phi_{\Gamma}(\delta, \tau)}{\partial \delta}$$
 (2)

$$C_{p}(\delta,\tau) = R \left[ -\tau^{2} \left( \frac{\partial^{2} \Phi_{o}}{\partial \tau^{2}} + \frac{\partial^{2} \Phi_{r}}{\partial \tau^{2}} \right) + \frac{\left( 1 + \delta \frac{\partial \Phi_{r}(\delta,\tau)}{\partial \delta} - \delta \tau \frac{\partial^{2} \Phi_{r}(\delta,\tau)}{\partial \delta \partial \tau} \right)^{2}}{1 + 2\delta \frac{\partial \Phi_{r}(\delta,\tau)}{\partial \delta} + \delta^{2} \frac{\partial^{2} \Phi_{r}(\delta,\tau)}{\partial \delta^{2}}} \right]$$

$$(3)$$

where  $\Phi$  is the dimensionless Helmholtz energy;  $\Phi_0$  is the Helm-

$$\mu(\rho, T) = \mu_0(T) + \Delta\mu(\rho, T) + \Delta\mu_0(\rho, T) \tag{5}$$

$$\lambda(\rho, T) = \lambda_{0}(T) + \Delta\lambda(\rho, T) + \Delta\lambda_{c}(\rho, T)$$
(6)

where  $\mu$  is the viscosity of  $CO_2$ ,  $N \cdot s/m^2$ ;  $\lambda$  is the thermal conductivity of  $CO_2$ ,  $W/(m \cdot K)$ ;  $\mu_0$  and  $\lambda_0$  are the viscosity and thermal conductivity in the zero-density limit;  $\Delta \mu$  and  $\Delta \lambda$  represent the increase in the viscosity and thermal conductivity at elevated density over the dilute gas value;  $\Delta_c \mu$  and  $\Delta_c \lambda$  are the increments of viscosity and thermal conductivity as the  $CO_2$  fluid is near the critical point.

# 2.2. The computational fluid dynamic equations

$$C_{\mathbf{J}}(\delta,\tau) = R_{\rho} \frac{-\left(\delta \frac{\partial \Phi_{\mathbf{r}}(\delta,\tau)}{\partial \delta} + \delta^{2} \frac{\partial^{2} \Phi_{\mathbf{r}}(\delta,\tau)}{\partial \delta^{2}} + \delta \tau \frac{\partial^{2} \Phi_{\mathbf{r}}(\delta,\tau)}{\partial \delta \partial \tau}\right)}{\left(1 + \delta \frac{\partial \Phi_{\mathbf{r}}(\delta,\tau)}{\partial \delta} - \delta \tau \frac{\partial^{2} \Phi_{\mathbf{r}}(\delta,\tau)}{\partial \delta \partial \tau}\right)^{2} - \tau^{2} \left(\frac{\partial^{2} \Phi_{\mathbf{o}}(\delta,\tau)}{\partial \tau^{2}} + \frac{\partial^{2} \Phi_{\mathbf{r}}(\delta,\tau)}{\partial \tau^{2}}\right) \left(1 + 2\delta \frac{\partial \Phi_{\mathbf{r}}(\delta,\tau)}{\partial \delta} + \delta^{2} \frac{\partial^{2} \Phi_{\mathbf{r}}(\delta,\tau)}{\partial \delta^{2}}\right)}$$

$$(4)$$

holtz energy for ideal gas;  $\Phi_{\Gamma}$  is the Helmholtz energy for the residual fluid part;  $\delta$  is ratio of the fluid densities under standard conditions and at the critical point,  $\delta = \rho/\rho_c$ ;  $\rho_c$  is the gas density at the critical point, kg/m³;  $\tau$  is ratio of the temperature under standard conditions and at the critical point,  $\tau = T_c/T$ ;  $T_c$  is the temperature at the critical point, K; R is gas constant, J/(kg·K).

The viscosity and thermal conductivity of the CO<sub>2</sub> fluid are usually calculated by the model of Fenghour (Fenghour et al., 1998):

Considering the compressible property of SC-CO<sub>2</sub>, we adopted the three-dimensional compressible fluid equations to calculate the mass, momentum, and energy conservation equations (Versteeg and Malalasekera, 2007).

$$\frac{\partial \rho}{\partial t} + \frac{\partial (\rho u)}{\partial x} + \frac{\partial (\rho v)}{\partial y} + \frac{\partial (\rho w)}{\partial z} = 0 \tag{7}$$

$$\frac{\partial(\rho u)}{\partial t} + \frac{\partial(\rho u u)}{\partial(x)} + \frac{\partial(\rho u w)}{\partial(y)} + \frac{\partial(\rho u w)}{\partial(z)} \\
= \frac{\partial}{\partial x} \left( \mu \frac{\partial u}{\partial x} \right) + \frac{\partial}{\partial y} \left( \mu \frac{\partial u}{\partial y} \right) + \frac{\partial}{\partial z} \left( \mu \frac{\partial u}{\partial z} \right) - \frac{\partial p}{\partial x} + S_{i} \frac{\partial(\rho v)}{\partial t} + \frac{\partial(\rho v u)}{\partial(x)} + \frac{\partial(\rho v w)}{\partial(y)} + \frac{\partial(\rho v w)}{\partial(z)} \\
= \frac{\partial}{\partial x} \left( \mu \frac{\partial v}{\partial x} \right) + \frac{\partial}{\partial y} \left( \mu \frac{\partial v}{\partial y} \right) + \frac{\partial}{\partial z} \left( \mu \frac{\partial v}{\partial z} \right) - \frac{\partial p}{\partial x} + S_{i} \frac{\partial(\rho w)}{\partial t} + \frac{\partial(\rho w u)}{\partial(x)} + \frac{\partial(\rho w w)}{\partial(y)} + \frac{\partial(\rho w w)}{\partial(z)} \\
= \frac{\partial}{\partial x} \left( \mu \frac{\partial w}{\partial x} \right) + \frac{\partial}{\partial y} \left( \mu \frac{\partial w}{\partial y} \right) + \frac{\partial}{\partial z} \left( \mu \frac{\partial w}{\partial z} \right) - \frac{\partial p}{\partial x} + S_{i}$$
(8)

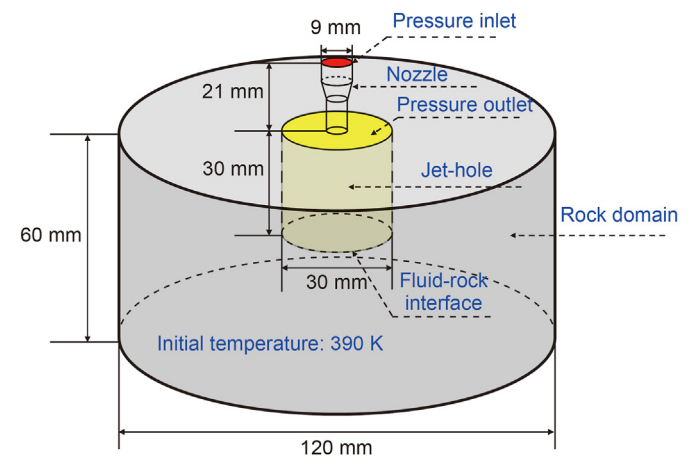


Fig. 2. The geometric model of computation zones.

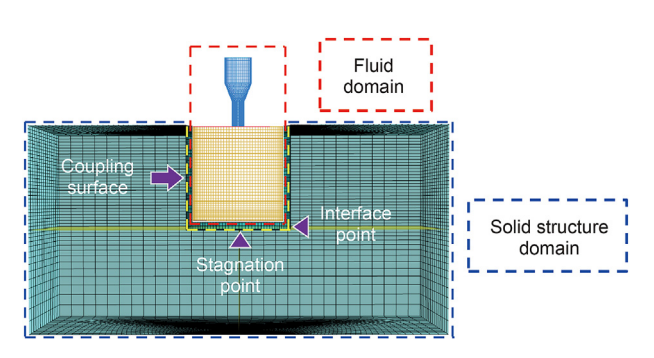


Fig. 3. Schematic diagram of fluid-solid coupling.

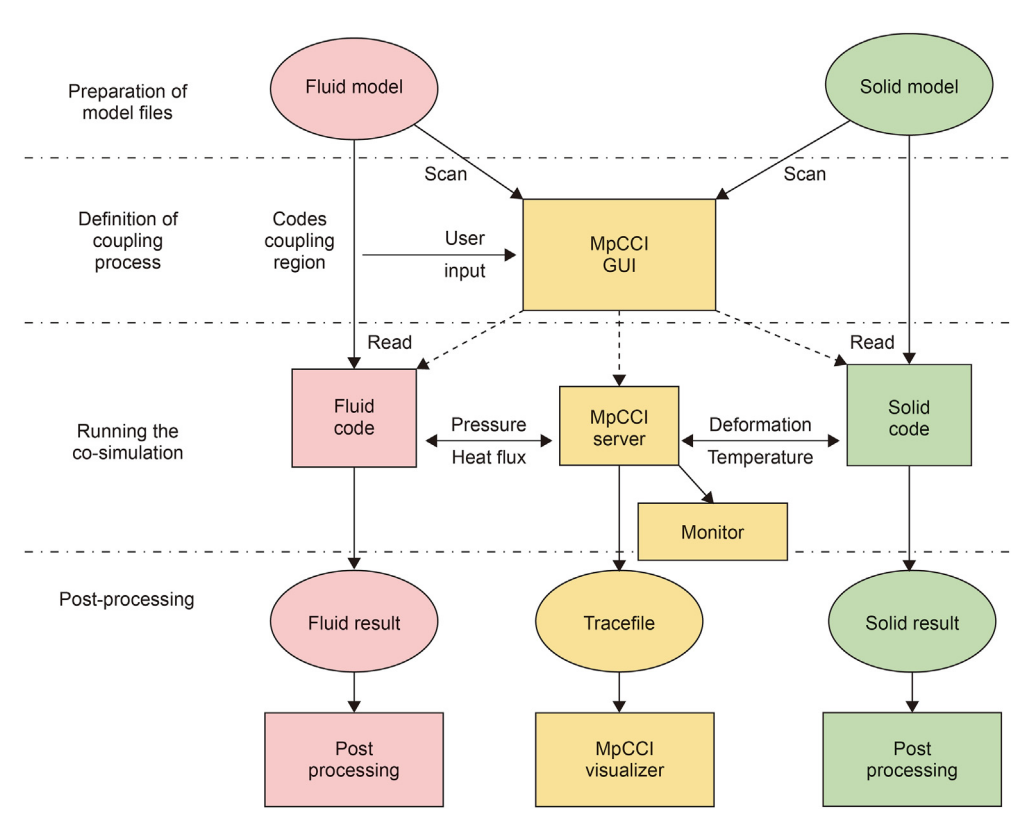


Fig. 4. Co-simulation with MpCCI: Overview of the simulation process.

**Table 1** Parameters of SC-CO<sub>2</sub> and water in the modeling.

Modeling parameters		SC-CO <sub>2</sub>	Water
Inlet pressure, MPa		40	40
Outlet pressure, MPa		30	30
Fluid temperature, K		320	320
Physical properties	Viscosity, Pa·s	Determined by the real-gas-model	1.003E-5
	Density, kg/m <sup>3</sup>		998.2
	Thermal conductivity, W/(m·K)		0.6
	Heat capacity, kJ/(kg·K)		4.182

$$\frac{\partial(\rho T)}{\partial t} + \frac{\partial(\rho u T)}{\partial(x)} + \frac{\partial(\rho v T)}{\partial(y)} + \frac{\partial(\rho w T)}{\partial(z)} = S_{T} + \frac{\partial}{\partial x} \left( \frac{k_{h}}{C_{p}} \frac{\partial T}{\partial x} \right) + \frac{\partial}{\partial y} \left( \frac{k_{h}}{C_{p}} \frac{\partial T}{\partial y} \right) \\
+ \frac{\partial}{\partial z} \left( \frac{k_{h}}{C_{p}} \frac{\partial T}{\partial z} \right) \tag{9}$$

where u, v, w are the fluid velocities at the coordinate axis direction of x, y, z, m/s;  $\mu$  is the dynamic viscosity,  $Pa \cdot s$ ; p is the fluid pressure, Pa; T is the temperature, K;  $k_h$  is the thermal conductivity;  $S_i$  and  $S_T$  are the source terms of the momentum and energy conservation equations.

# 3. Geometric and numerical model

# 3.1. Model assumption

In this simulation, we assumed that the vicinity of the wellbore had been filled with  $CO_2$  during jet fracturing (Shi et al., 2019). Under geothermal reservoir conditions, the temperature and pressure are commonly high above the critical point at 31.1 °C and

7.38 MPa. Therefore, CO<sub>2</sub> was assumed under a single phase in the supercritical state. According to previous studies (Chen et al., 2019), the seeping flow pattern of SC-CO<sub>2</sub> in geothermal reservoir pores can be simplified to Darcy's model. During the abrasive jet perforation process, rock and particles' impact was considered within the elastic collision. Furthermore, the rock was regarded as homogeneous and isotropic. And there was no large rock deformation during jet impingement.

**Table 2**Carbonate rock model basic parameters (Xu et al., 2020).

Modeling parameter	Value
Density, kg/m <sup>3</sup>	2600
Temperature, K	390
Elastic modulus, GPa	50
Poisson	0.30
Porosity	0.05
Permeability, mD	2.96
Coefficient of thermal expansion, K <sup>-1</sup>	2E-6
Specific heat capacity, J/(kg·K)	880
Heat transfer rate, $W/(m \cdot K)$	1.57

#### 3.2. Geometric model and boundary conditions

As shown in Fig. 2, a three-dimensional geometry model was built to simulate the  $SC-CO_2$  jet fracturing process. The model can be divided into the rock domain and the jet-hole domain. The rock domain is confined in a cylinder with 120 mm diameter and 60 mm length. At the rock center, the jet hole is simplified as a cylinder with 30 mm diameter and 30 mm height. The  $SC-CO_2$  and abrasive particles are pumped into the nozzle, flowing through the perforation cavity, impacting the bottom surface, a small portion of  $SC-CO_2$  seeping into the rock pores and most of them flowing out to the annulus. The specific information of the geometric model is shown in Fig. 2.

Following the field applications, the boundaries of the jet hole were set as pressure inlet and pressure outlet. The interface of fluid and rock was set as a coupled wall to transform the heat flux and pressure between the two parts. The bottom and side surface of the rock domain were set as constant pressure boundary conditions. The value was equal to the formation pressure (20 MPa). Other boundaries were set as the adiabatic wall during calculation.

# 3.3. Coupling method

According to Fig. 3, the SC-CO<sub>2</sub> jet fracturing impingement simulation is a complex process that contains two parts. The fluid jet impingement effect in the fluid domain and the stress response of carbonate rock in the solid structure domain. Meanwhile, the thermal effect also needs to be considered in the geothermal reservoir. A loose coupling method was adopted to calculate the interaction between two parts, which is achieved by exchanging the coupling data across the fluid-solid interfaces (Wu et al., 2019). In this simulation, we adopted the MpCCI (mesh-based parallel code coupling interface) as the coupling connector to link the fluid domain (Fluent) and solid structure domain (Abaqus) together. MpCCI is a multi-physics professional mesh coupling interface software developed by the Fraunhofer Institute for Algorithms and Scientific Computing (Zhai et al., 2021). It creates a channel to exchange the data of different simulation codes between meshes. MpCCI has been widely used to calculate the multi-physics coupling simulation in many industry fields (Li et al., 2020). For the application in jet impingement, Wu et al. (2019) conducted the

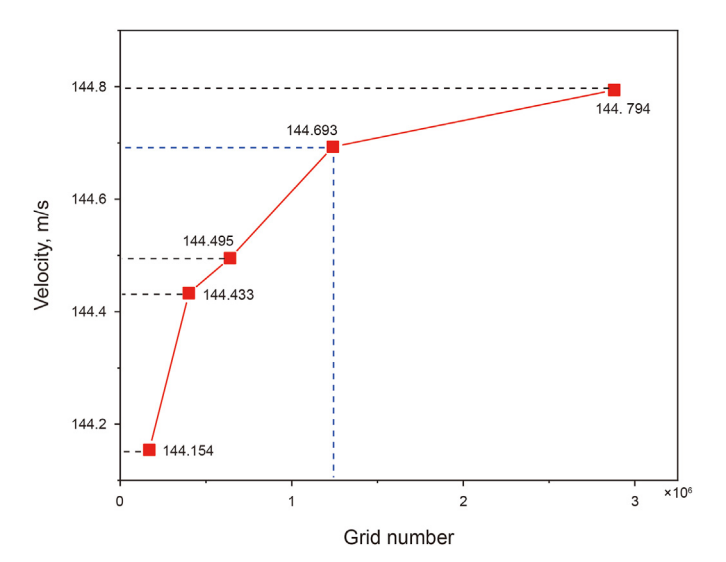


Fig. 6. Sensitivity of mesh number.

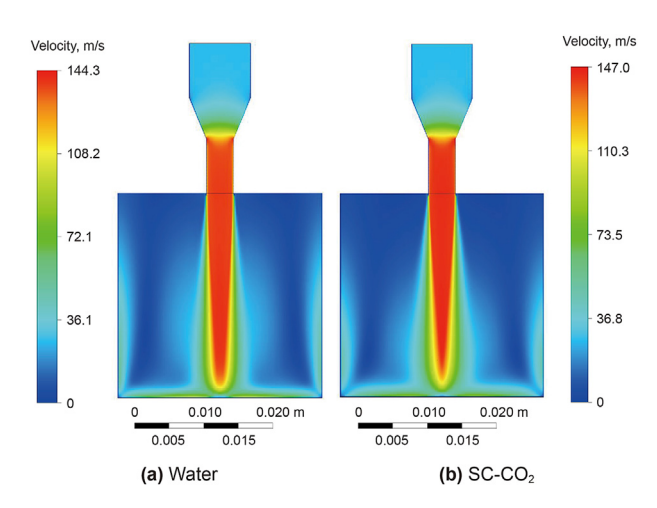
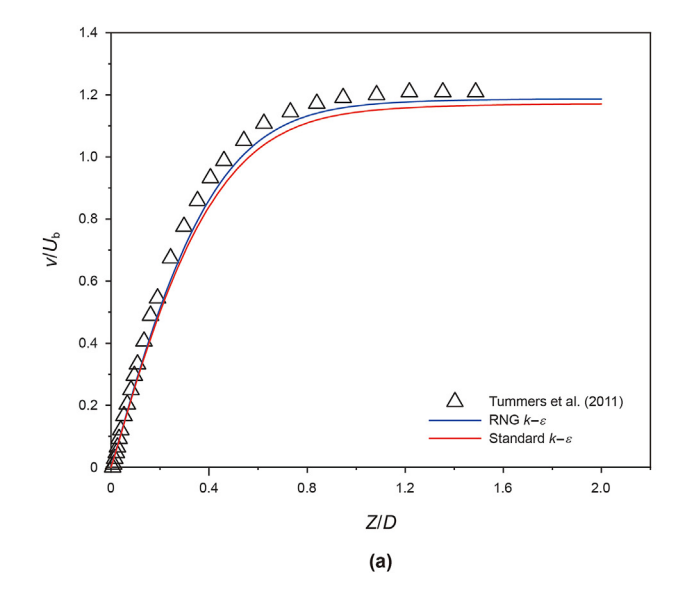


Fig. 7. Velocity contours of (a) water jet and (b) SC-CO<sub>2</sub> jet.



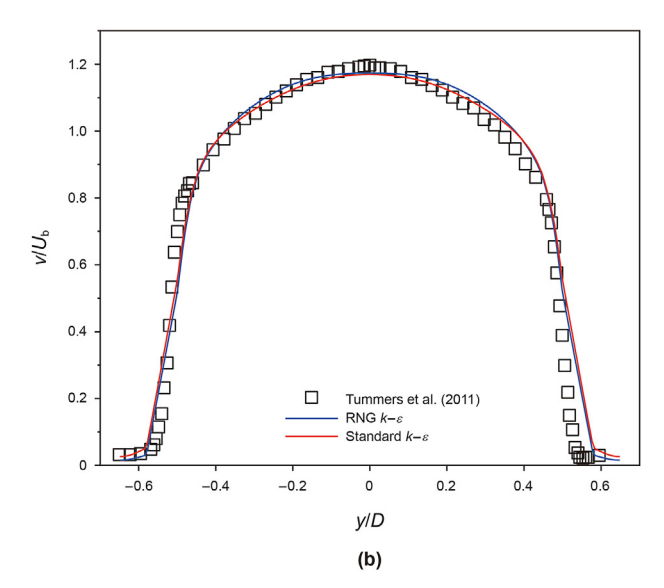


Fig. 5. Comparison between simulation results and experimental data.

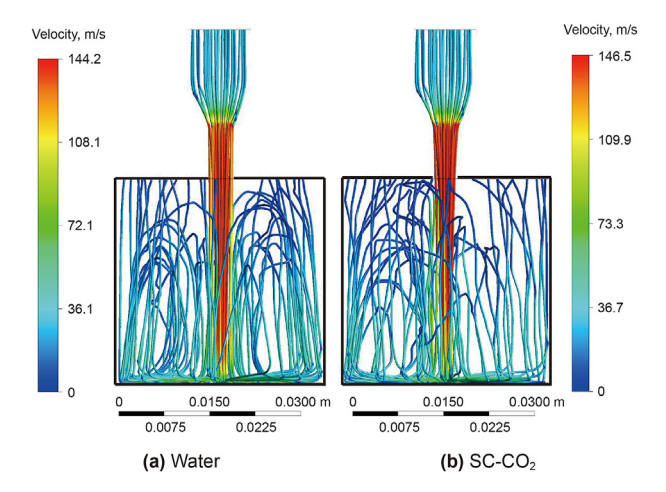


Fig. 8. Particle trajectories of (a) water jet and (b) SC-CO<sub>2</sub> jet.

fluid-thermo-mechanical coupling model of liquid nitrogen ( $LN_2$ ) jet impingement based on MpCCI.

The detailed coupling process of MpCCI for fluid-structure interaction (FSI) is illustrated in Fig. 4. Furthermore, the coupling data should satisfy Eq. (10):

$$\begin{split} P_{\mathbf{f}}(x,y,z,t) \cdot n_{\mathbf{f}} &= P_{\mathbf{s}}(x,y,z,t) \cdot n_{\mathbf{s}} \\ d_{\mathbf{f}}(x,y,z,t) &= d_{\mathbf{s}}(x,y,z,t) \\ T_{\mathbf{f}}(x,y,z,t) &= T_{\mathbf{s}}(x,y,z,t) \\ h_{\mathbf{f}} \frac{\partial T_{\mathbf{f}}}{\partial n_{\mathbf{f}}}(x,y,z,t) &= q_{\mathbf{f}} = q_{\mathbf{s}} = h_{\mathbf{s}} \frac{\partial T_{\mathbf{s}}}{\partial n_{\mathbf{s}}}(x,y,z,t) \end{split} \tag{10}$$

where P, d, T, h, q represent the pressure, deformation, temperature, heat conduction coefficient, and heat flux, respectively; n is the normal vector of the coupling surface; subscripts f and g indicate the fluid domain and solid domain.

The pressure and heat flux data on the coupling surface are transferred from the fluid domain to the solid structure domain every iteration. After the solid domain calculates, the deformation and temperature data are transmitted back to the fluid domain with new boundary conditions. The process mentioned above is

constantly repeated and recycled before reaching the predefined time in the calculation. The mesh near the coupled surface was refined on both sides for high accuracy. The dynamic mesh method in Fluent was adopted, as the impacted surface would deform slightly after each iteration.

# 3.4. Fluid and solid domain modeling

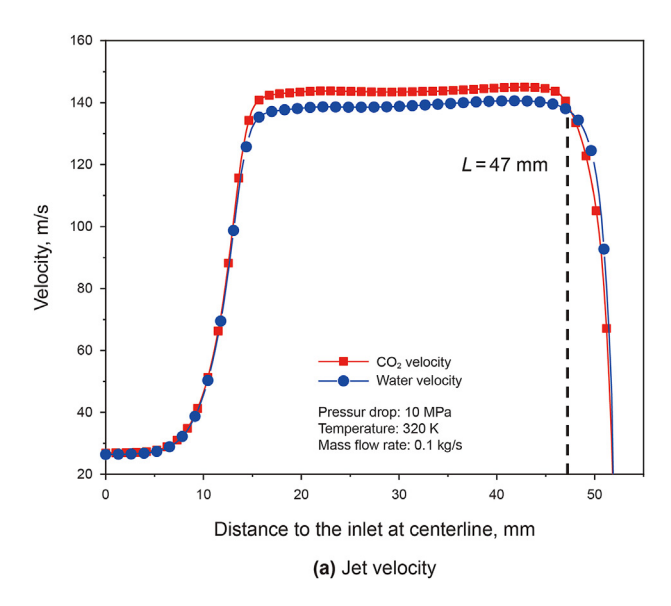
# 3.4.1. Perforation fluid flow model

In calculating impinging jet flow, the flow field in the perforation cavity is a high Reynolds number region with drastic vortex motion. This study adopted the RNG  $k-\varepsilon$  model to calculate the RANS equations, which are widely used by scholars (Zhang et al., 2018a) to solve turbulence with significant vortex motion. As the physical property of SC-CO<sub>2</sub> is susceptible to pressure and temperature, we employed the NIST real-gas model and the coupled algorithm to address the issue of thermophysical property variations. The timestep is fixed as 0.1 ms. Detailed fluid parameters are illustrated in Table 1.

For calculating the abrasive jet flow field, two methods are commonly employed. One is to treat the solid phase as a continuous medium or pseudo-fluid, and the other method is to treat the solid phase as a discrete phase medium (Chang et al., 2019). In this model, due to the low particle density in jet flow, the discrete phase model (DPM) was introduced into the fluid domain. The model solves the Navier-Stokes equations in the Euler framework for the continuous phase (fluid) and calculates the orbital particle equation in the Lagrange framework for abrasive particles. Besides, to demonstrate the destruction effect of particles, the erosion model was activated to analyze the degree of particle erosion qualitatively. In the Cartesian coordinate system, the force balance equation for a single abrasive particle can be expressed as (Bennon and Incropera, 1987):

$$\frac{\mathrm{d}u_{\mathrm{p}}}{\mathrm{d}t} = F_{D}\left(u_{\mathrm{f}} - u_{\mathrm{p}}\right) + \frac{g\left(\rho_{\mathrm{p}} - \rho_{\mathrm{f}}\right)}{\rho_{\mathrm{p}}} + F_{x} \tag{11}$$

where  $F_{\rm D}(u_{\rm f}-u_{\rm p})$  is the drag force of the particle;  $\frac{{\rm g}(\rho_{\rm p}-\rho_{\rm f})}{\rho_{\rm p}}$  is the gravity item;  $F_{\rm x}$  is the additional force item;  $u_{\rm p}$ ,  $u_{\rm f}$  are the velocities of particle and fluid, m/s;  $\rho_{\rm p}$ ,  $\rho_{\rm f}$  are the densities of particle and fluid,



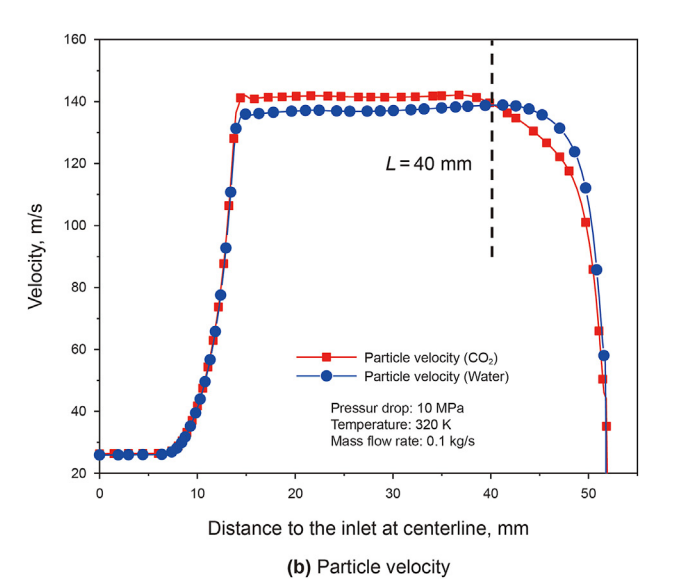


Fig. 9. Velocity distribution at the centerline.

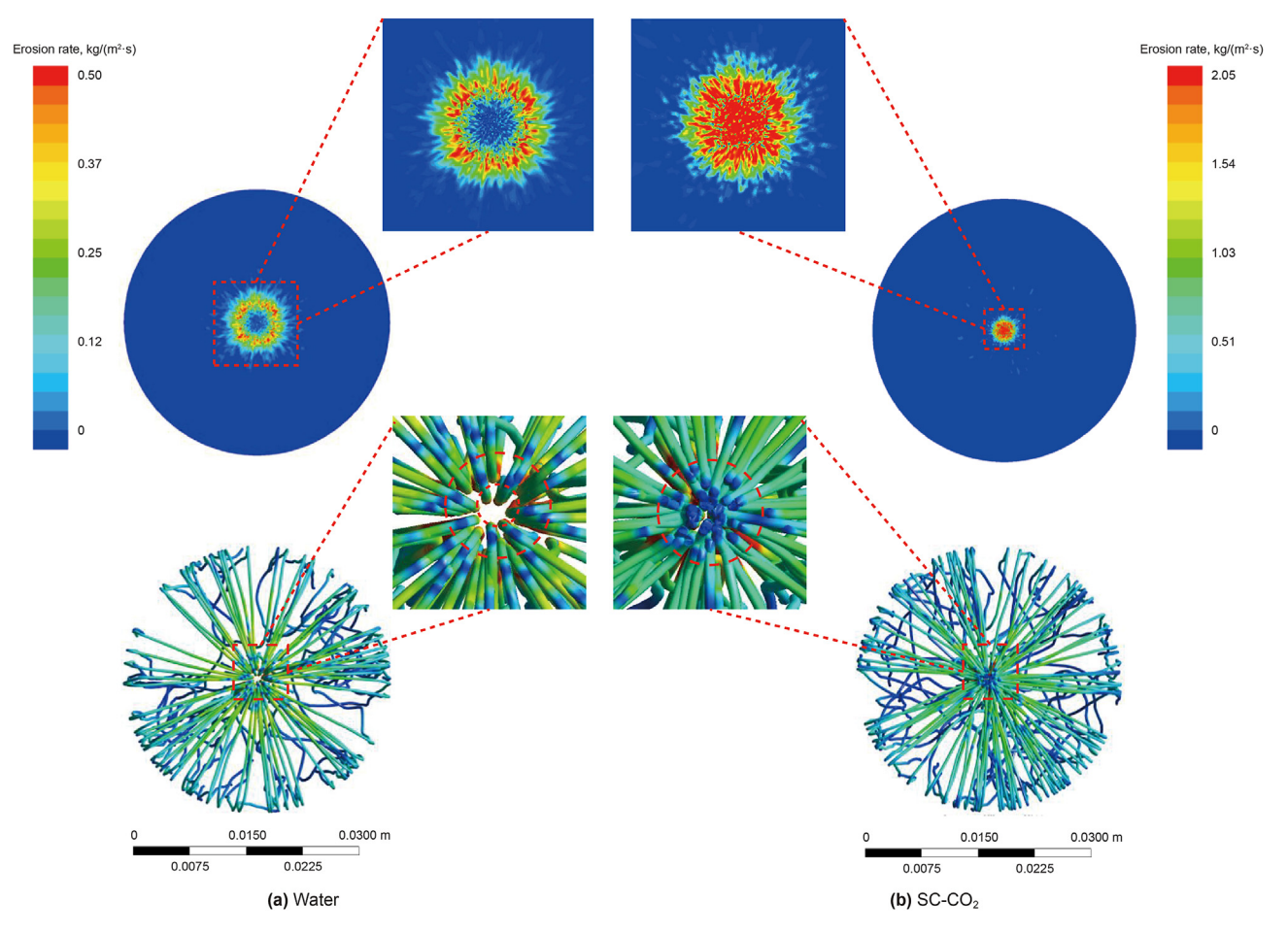


Fig. 10. Erosion rate contours and particles trajectory of (a)water and (b) SC-CO2 at the bottom surface.

 $kg/m^3$ .

The erosion model can be calculated by the equation as below (Edwards et al., 2000):

$$R_{\text{erosion}} = \sum_{p=1}^{Np} \frac{m_{\text{p}} C(d_{\text{p}}) f(\alpha) v_{\text{p}}^{b(\nu)}}{A_{\text{face}}}$$
(12)

where  $N_p$  is the number of particles;  $m_p$  is the mass flux;  $C(d_p)$  is the

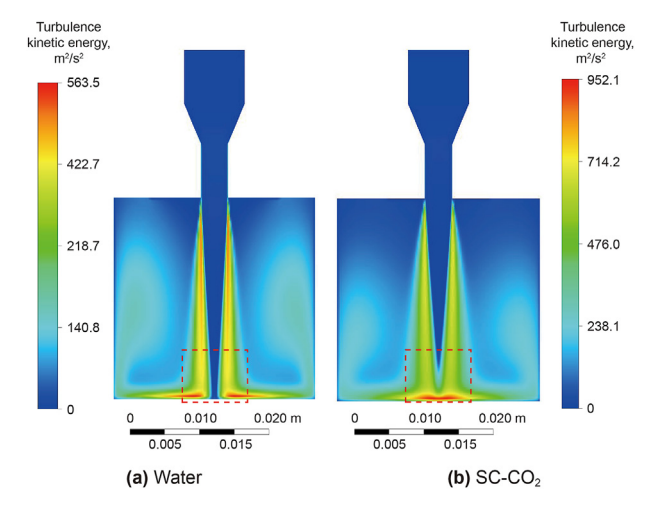


Fig. 11. Turbulence kinetic energy contours of (a) water and (b) SC-CO<sub>2</sub>.

particle size function;  $\alpha$  is the Impact angle;  $f(\alpha)$  is the impact angle function;  $v_p$  is the particle velocity; b(v) is the velocity function;  $A_{\text{face}}$  is the wall area.

#### 3.4.2. Porous flow model

The bottom carbonate rock is set as homogeneous porous media with relatively low permeability. We adopted the Darcy-Brinkman-Forchheimer model (Vafai and Tien, 1981) to calculate the flow transport in porous media. The continuity and momentum governing equations can be expressed in Eqs. (13) and (14).  $S_i$  in Eq. (15) represents the flow resistance source term. As the flow velocity  $u_i$  is small enough in the rock media, the model can be simplified to the Darcy model (Zhang et al., 2018b).

$$\frac{\partial \left(\phi \rho_{\rm f}\right)}{\partial t} + \nabla \left(\rho_{\rm f} u_{\rm i}\right) = 0 \tag{13}$$

$$\frac{\partial \left(\rho_{f}\frac{u_{i}}{\phi}\right)}{\partial t} + \nabla \left(\rho_{f}\frac{u_{i}}{\phi} \cdot \frac{u_{i}}{\phi}\right) = -\nabla P + \nabla \mu_{f} \nabla \frac{u_{i}}{\phi} + S_{i}$$
(14)

$$S_{i} = -\frac{\mu_{f}}{K}u_{i} + C\frac{1}{2}\rho_{f}|u|u_{i}$$
 (15)

where  $\phi$  is the rock porosity;  $\rho_f$  is the fluid density, kg/m³;  $u_i$  is the fluid velocity in the i direction, m/s;  $\mu_f$  is the viscosity of fluid, Pa·s; P is the pressure, Pa; K is rock permeability, m².

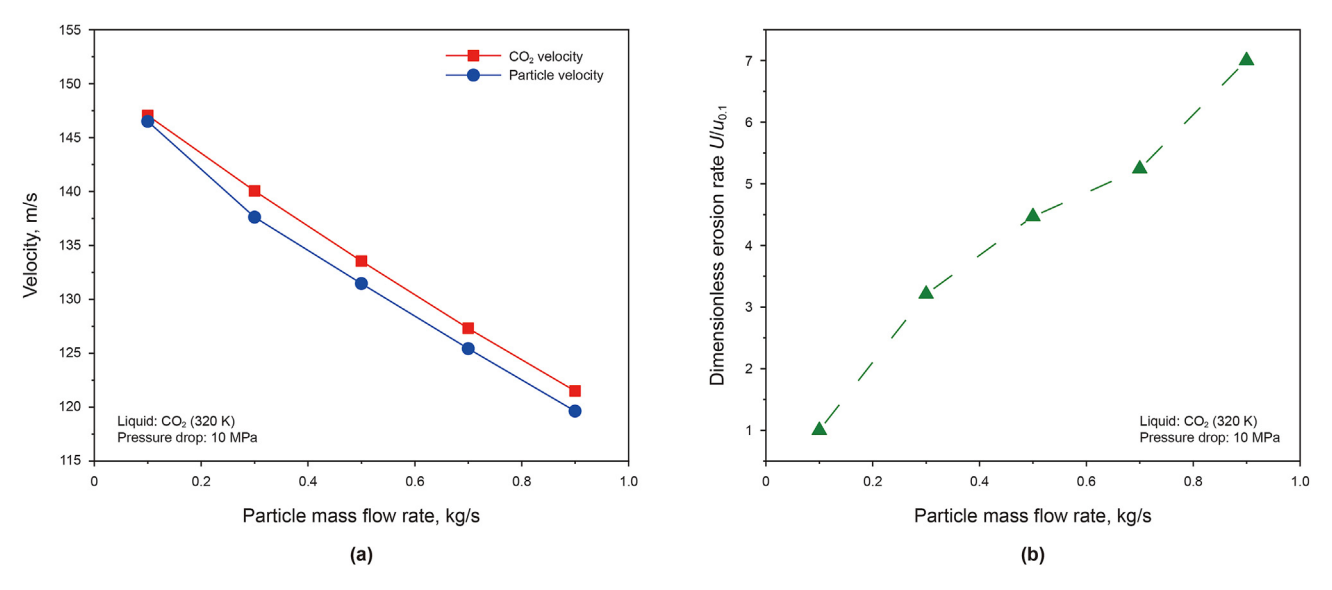


Fig. 12. The maximum jet velocity and dimensionless erosion rate distribution with different mass flow rates,

#### 3.4.3. Solid domain model

The rock domain was set as homogenous carbonate rock in the solid domain. The effect of temperature and dilatation of rock were taken into account. The physical properties of carbonate rock were taken from the previous study, as shown in Table 2. The jet impact stress and thermal stress need to be calculated simultaneously in the calculation process. Therefore, we adopted the coupled temperature-displacement solution step to calculate this fully coupled process. NLgeom (Nonlinear geometry) was turned on to take the geometric deformation into account. The timestep is fixed as 0.1 ms to match with the fluent domain.

#### 3.5. Model validation

Validation was conducted by comparing the results with the previous experimental data to confirm the model's accuracy. The experimental data of Tummers (Tummers et al., 2011) is widely adopted for validating the turbulent flow. Their experiments

investigated the turbulent impinging jet in a long straight pipe at a Reynolds number of 23000. We employed the RNG  $k-\varepsilon$  model and Standard  $k-\varepsilon$  model to simulate the velocity field under the experimental conditions. First, a pipe flow model was built to develop the turbulent flow adequately for better revivification with the experiment. And then, the fully developed pipe flow was imported into the nozzle as the inlet boundary condition using the "profile file". Fig. 5a and b shows the velocity comparison between simulation results and experimental data in the centerline and the velocity of the cross section which is 7 mm away from the outlet, respectively. The measured velocity is expressed in the dimensionless term  $v/U_{\rm b}$ , where v is the vertical velocity along the centerline and  $U_{\rm b}$  is the bulk velocity at the nozzle's exit. It can be observed that the numerical results agree well with the experimental data.

To guarantee the mesh independence of results, we calculated the velocity at the distance of 20 mm from the nozzle as the indicator (Fig. 6). It can be seen that when the grid number exceeds

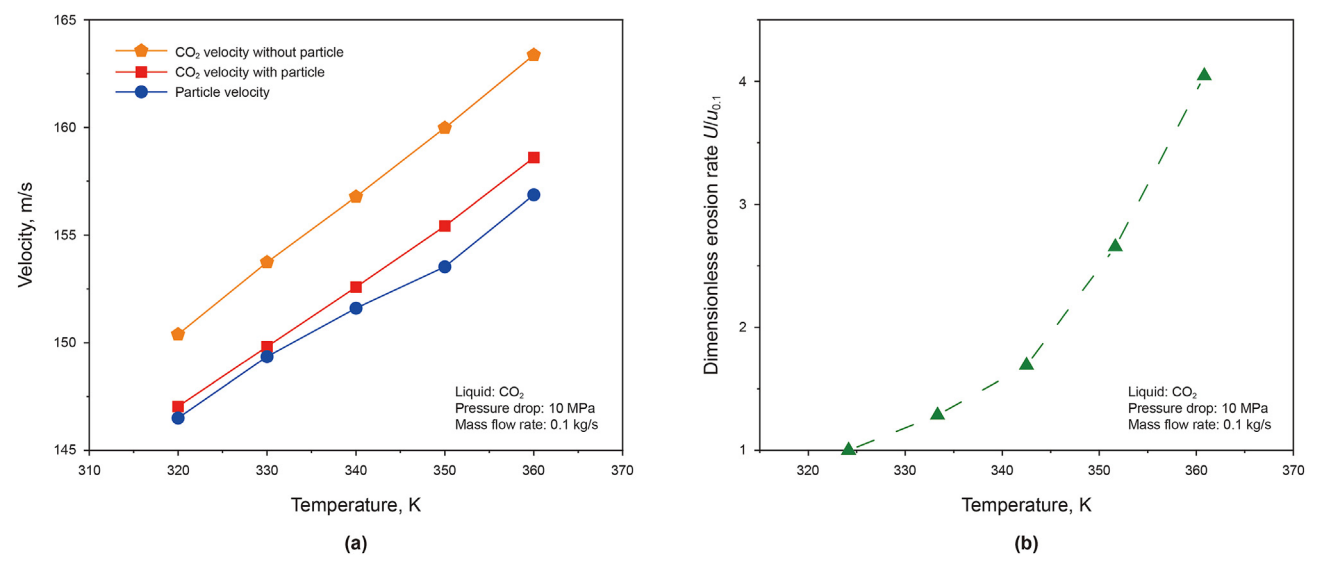


Fig. 13. The maximum velocity and dimensionless erosion rate at different temperatures.

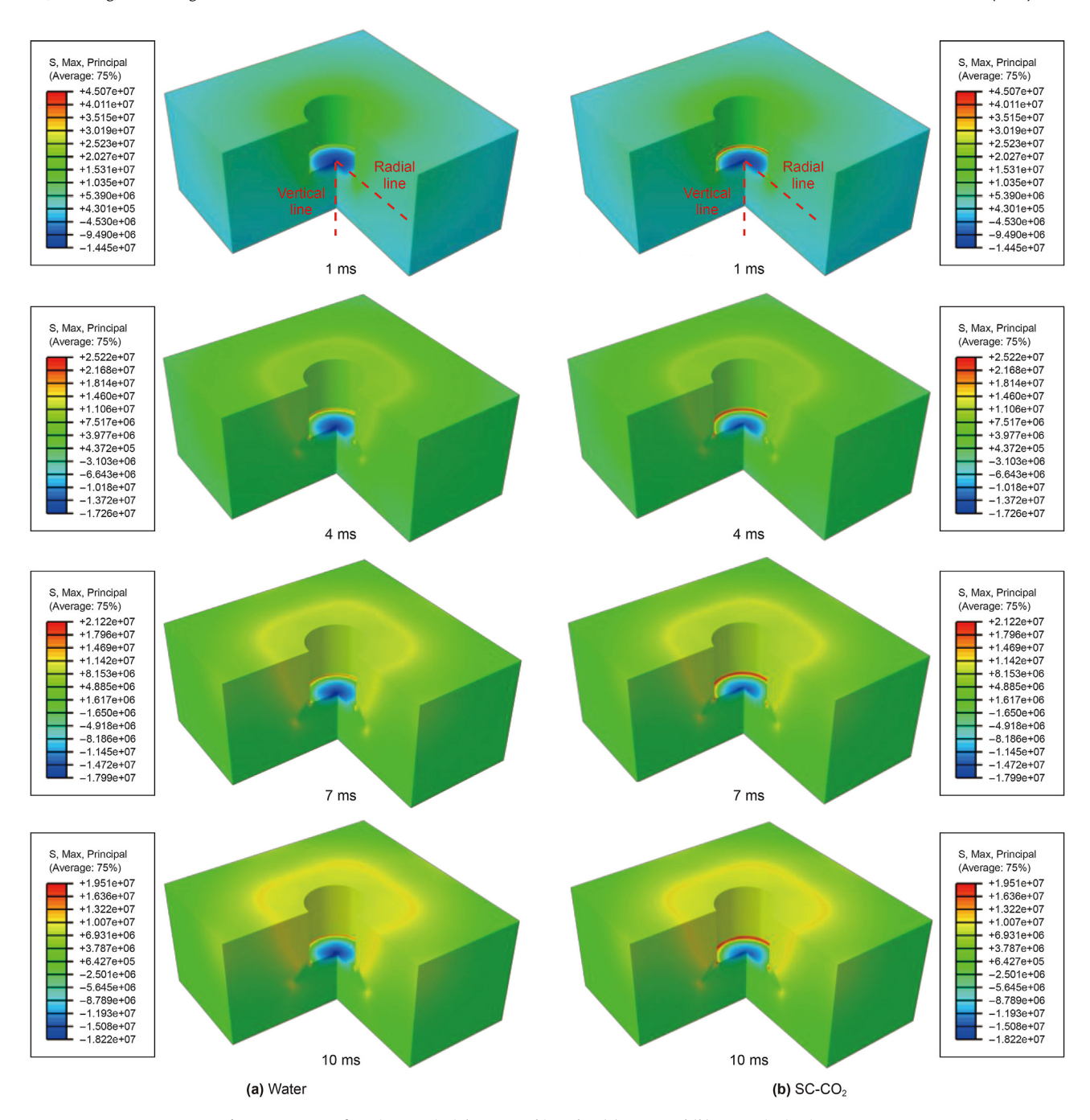


Fig. 14. Contours of maximum principle stress subjected to (a) water and (b) SC-CO $_2$  jet impingement.

1,240,000, the velocity has only a slight increase. Given the simulation accuracy and computation efficiency, a mesh scheme consisting of 1,313,856 cells was employed for the jet fracturing flow model.

# 4. Results and discussion

# 4.1. SC-CO<sub>2</sub> jet fracturing flow field

#### 4.1.1. Jet flow field and particle trajectory

Figs. 7 and 9a show the velocity contours and distribution of the water jet and SC-CO<sub>2</sub> jet, respectively. We found that the SC-CO<sub>2</sub> had a higher maximum jet velocity (147.4 m/s) than the water jet

(144.3 m/s) at the same pressure drop. It is mainly attributed to the rheologic properties of SC-CO<sub>2</sub>. Based on Bernoulli's principle, pressure potential energy converts to kinetic energy ( $\rho v^2/2$ ) in jet impingement. Due to lower density and viscosity, the velocity of SC-CO<sub>2</sub> showed a higher value than that of the water jet.

The fluid provides and accelerates the velocity of particles. Therefore, the high jet velocity commonly leads to a high particle velocity. As shown in Figs. 8 and 9b, the maximum particle velocity of SC-CO<sub>2</sub> (146.5 m/s) was 1.6% higher than that of the water jet (144.2 m/s), but it also dissipates more quickly. At about 40 mm from the inlet, the particle velocity of SC-CO<sub>2</sub> began to lower than that of water. This phenomenon is also mainly attributed to the rheologic properties of SC-CO<sub>2</sub>. From Eq. (11), we found that the

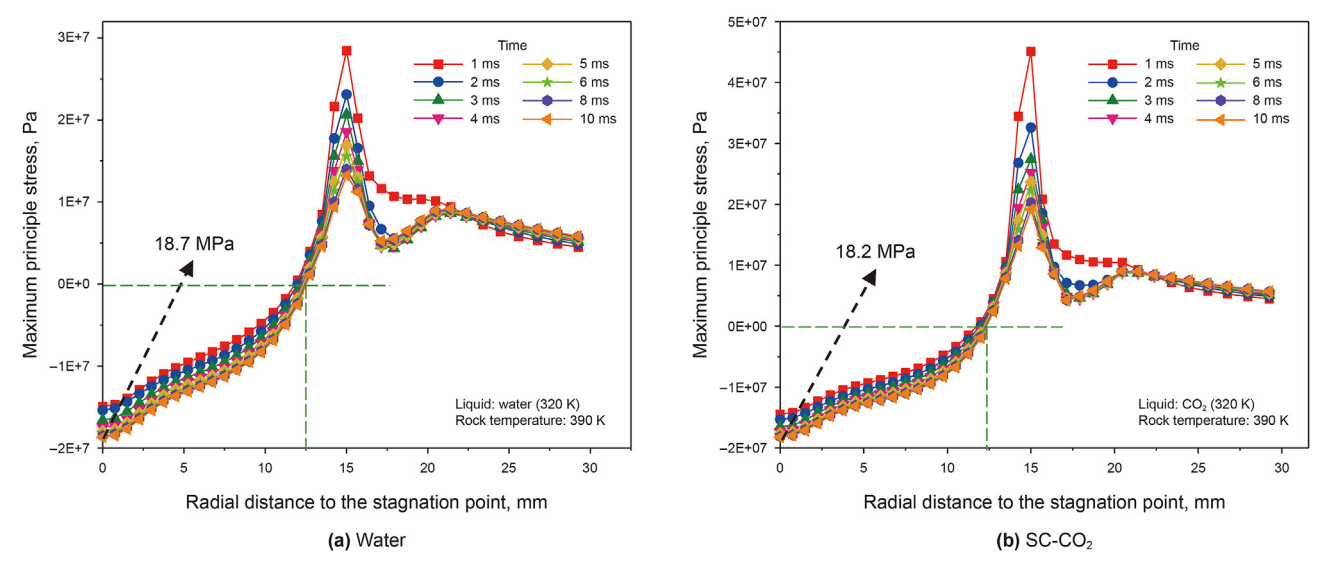


Fig. 15. Maximum principal stress distribution along the radial direction.

drag force  $F_D$  is highly related to the fluid viscosity and density. As mentioned before, the SC-CO<sub>2</sub> has a similar viscosity to the gas, which means a smaller drag force is carried on the particles. Hence, at the jet hole, the particle velocity of SC-CO<sub>2</sub> decreased more quickly.

# 4.1.2. Particle erosion rate

We introduced erosion analysis into the model, which is commonly employed in predicting pipe wear during fluid transport (Wang et al., 2019). We chose the widely used Generic erosion model (Edwards et al., 2000) as the governing equation (Eq. (12)) to calculate the erosion rate. It could help us to analyze the impact effect of particles qualitatively. Fig. 10 illustrates the particle erosion rate contours on the bottom surface of the water jet and SC-CO<sub>2</sub> jet, respectively. It can be observed that the two jets showed different erosion patterns and different degrees of damage. The water jet's erosion contour presented a ring shape, while SC-CO<sub>2</sub> presented a more centralized circle. The particles' trajectory also showed the same results. As shown in Fig. 10, there was no particle trajectory in

the center point on the bottom surface of the water jet compared with the SC-CO<sub>2</sub> jet.

This phenomenon is mainly attributed to the different fluid characteristics of the two jets. Fig. 11 illustrates the turbulence kinetic energy of the water jet and SC-CO2 jet, respectively. The turbulence kinetic energy is an indicator to present the turbulence intensity of the fluid. It can be seen that the turbulence intensity of the SC-CO<sub>2</sub> jet was much greater than the water jet at the nearby bottom surface. That meant the high SC-CO<sub>2</sub> jet velocity dissipated more significantly when the jet reached the bottom rock surface. In contrast, the water jet could accumulate at the stagnation point, preventing the later particles from impacting this area. That led to the different erosion patterns of the two jets. The centralized erosion pattern means a higher frequency of particle impact at the stagnation point, causing a high degree of damage. Thus, in applications, decreasing the particle density during the SC-CO2 perforation could achieve the same perforation effect as the water jet and simultaneously reduce the risk of sand plugging.

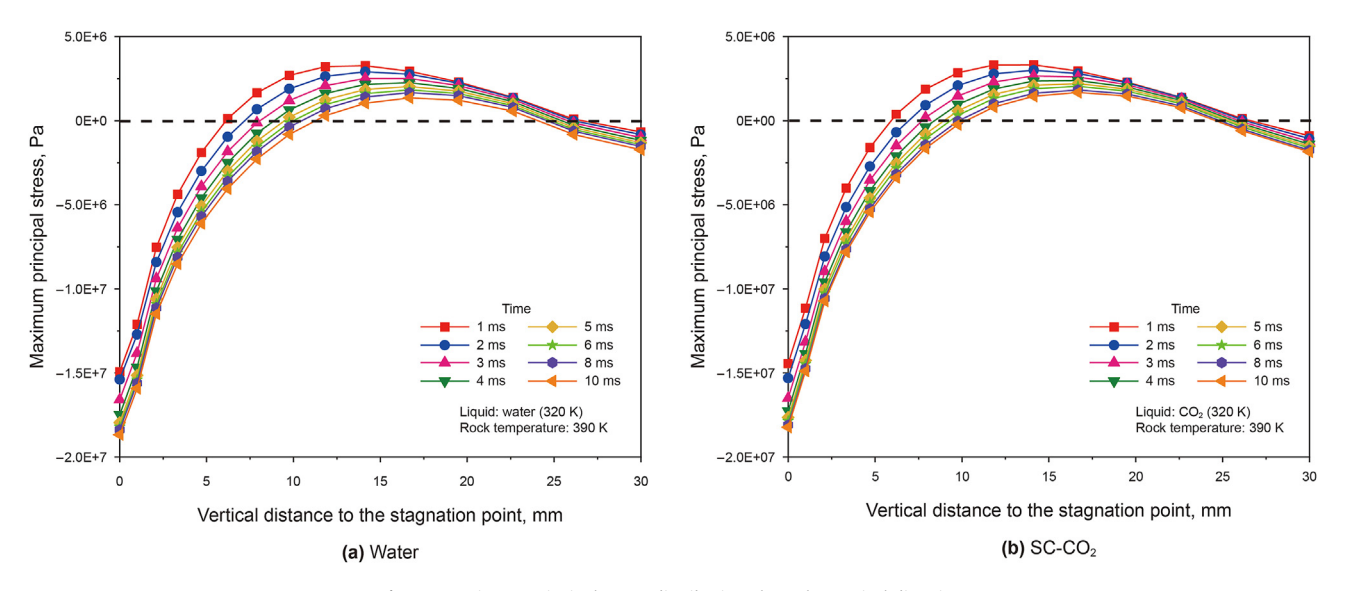


Fig. 16. Maximum principal stress distribution along the vertical direction.

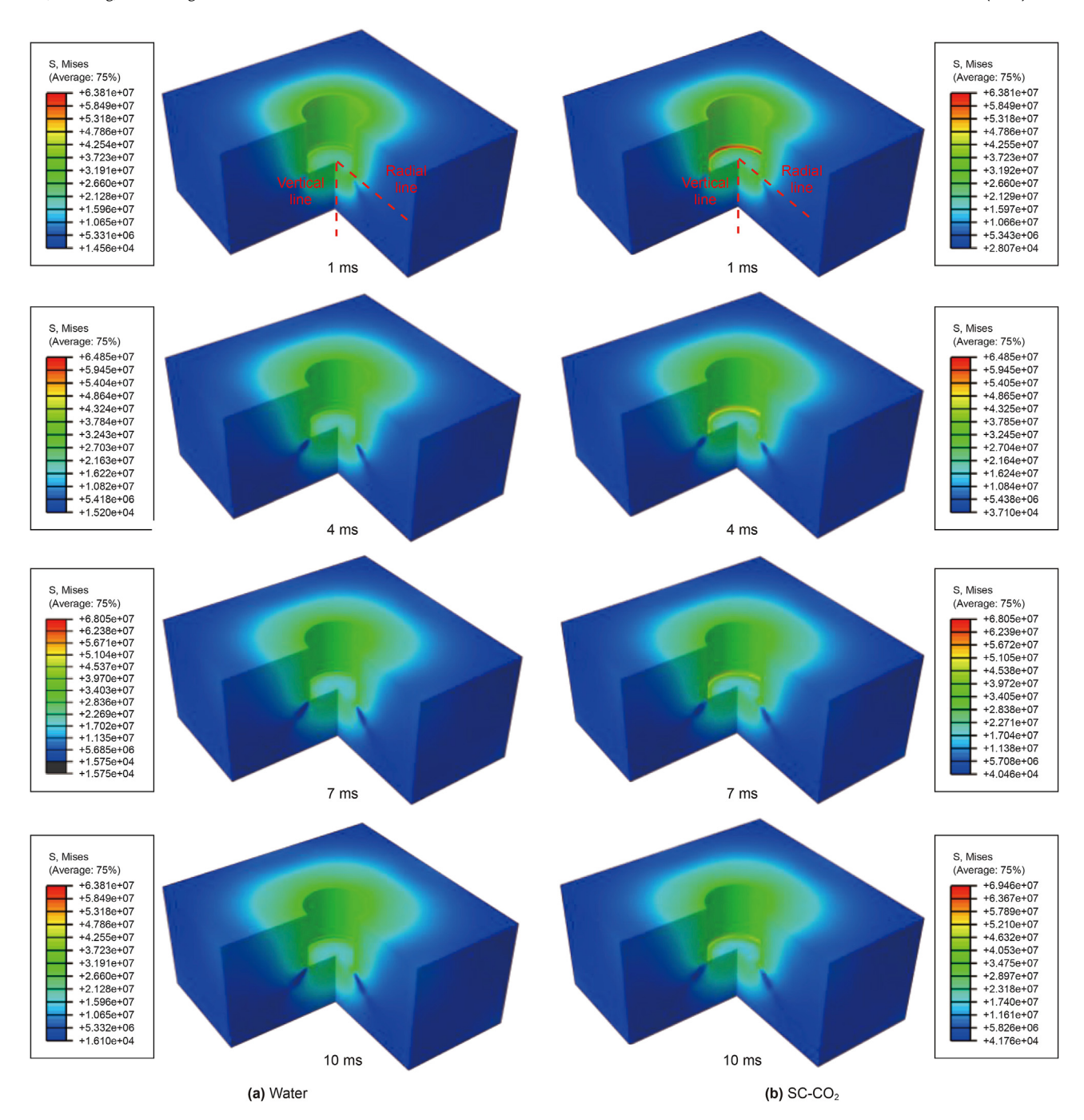


Fig. 17. Contours of Mises stress subjected to (a) water and (b) SC-CO2 jet impingement.

#### 4.1.3. Effect of mass flow rate and jet temperature

Fig. 12a and b illustrate the jet velocity and erosion rate change with different mass flow rates. The dimensionless term  $U/u_{0.1}$  was employed to indicate the erosion degree. U is the maximum erosion rate;  $u_{0.1}$  is the maximum erosion rate at particle mass flow rate equal to 0.1 kg/s. With the increase in particle mass flow rate, the maximum velocity of SC-CO<sub>2</sub> jet and particles decreased linearly from about 147 to 120 m/s. Moreover, the erosion rate increased about 7 times. The reason is that the high particle density needs a higher drag force to maintain the velocity. However, under the constant pressure drop conditions, the energy provided by the fluid was limited. The low velocity decreased the erosion rate. The high particle density increased the impacting frequency, and the higher

impacting frequency improved the erosion rate. In our model, the combination of two factors led to the increase in erosion rate.

Although the high erosion rate led to high perforation performance, the jet velocity could not maintain a high value. One of the critical factors for SC-CO<sub>2</sub> jet fracturing is the pressurization within the tunnel (Sheng et al., 2013). And the high-velocity jet flow provided the pressurization effect. Therefore, we needed to control the mass flow rate at a suitable value, performing well in perforation and maintaining high pressurization within the cavity.

Fig. 13 presents the maximum jet velocity and particle velocity distribution at different jet temperatures. It can be seen that with the increase in jet temperature, the jet velocity and particle velocity increased by about 12 m/s, and the particle erosion rate increased

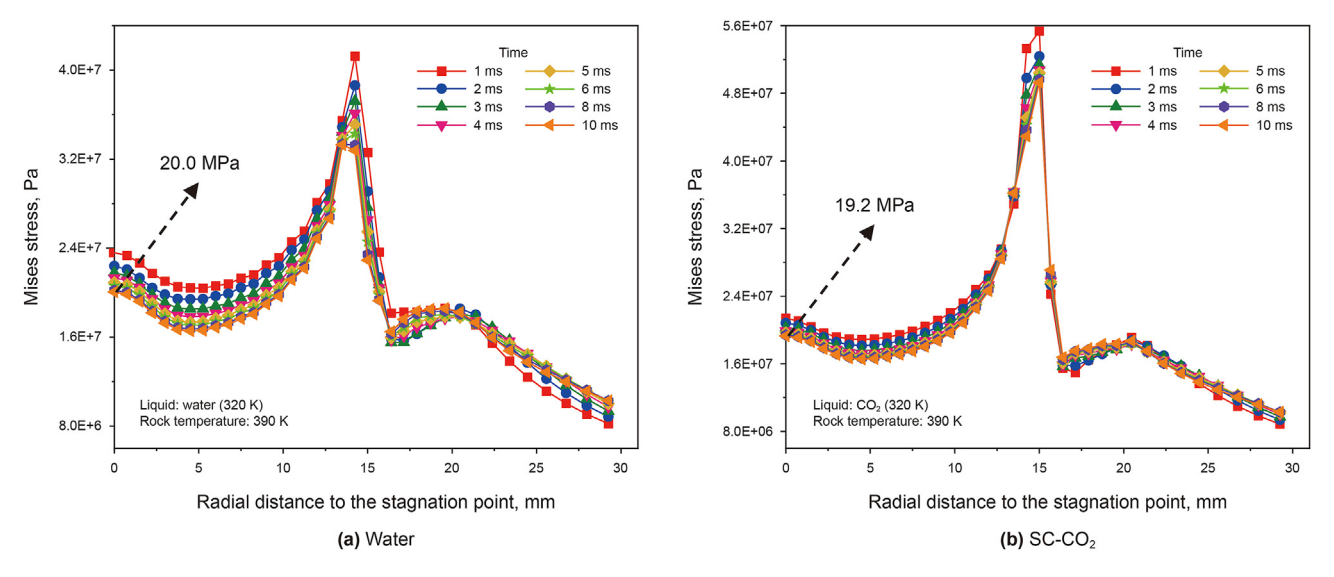
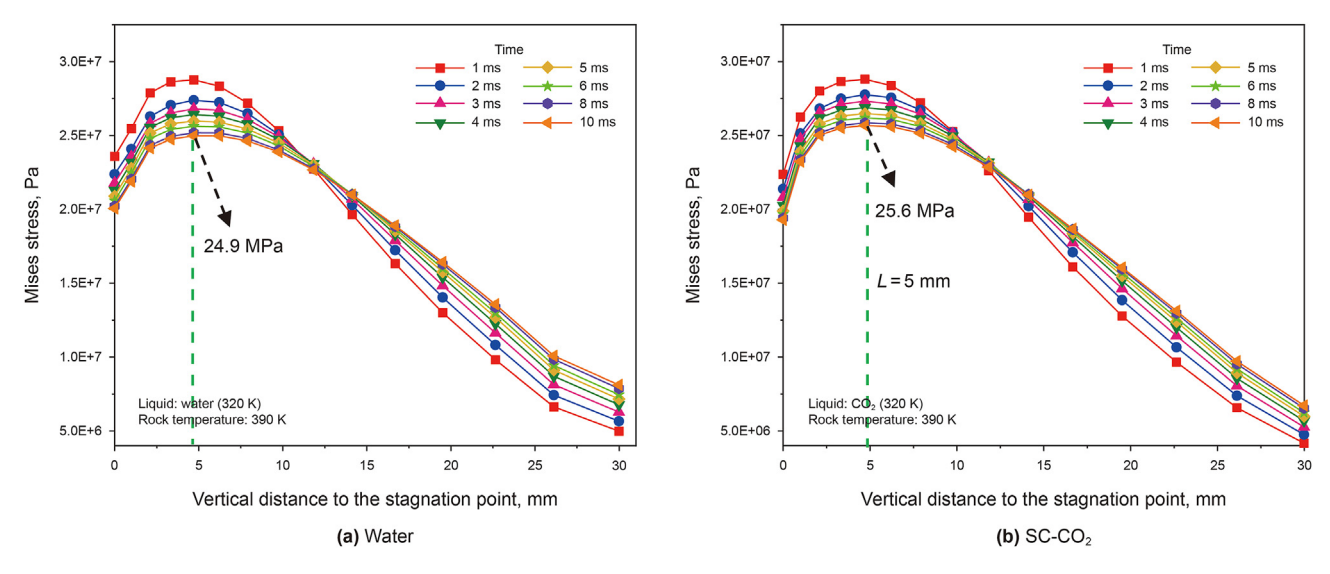


Fig. 18. Mises stress distribution along the radial direction: (a) water; (b) SC-CO<sub>2</sub>.



 $\textbf{Fig. 19.} \ \ \text{Maximum principal stress distribution along the vertical direction: (a) water; (b) \ \text{SC-CO}_2.$ 

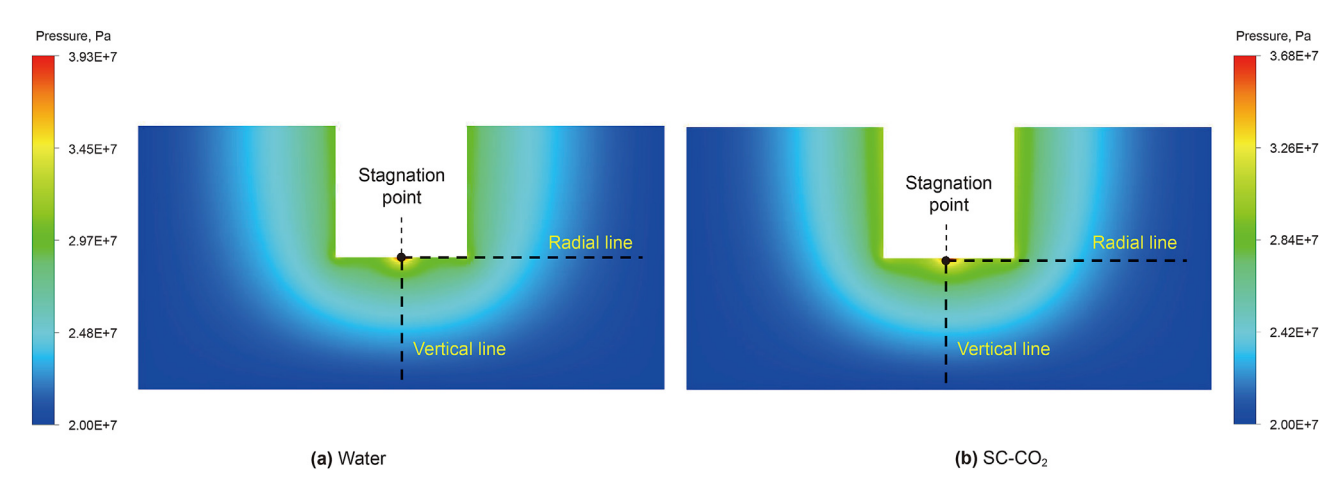


Fig. 20. The pore pressure contours of (a) water and (b) SC-CO<sub>2</sub>.

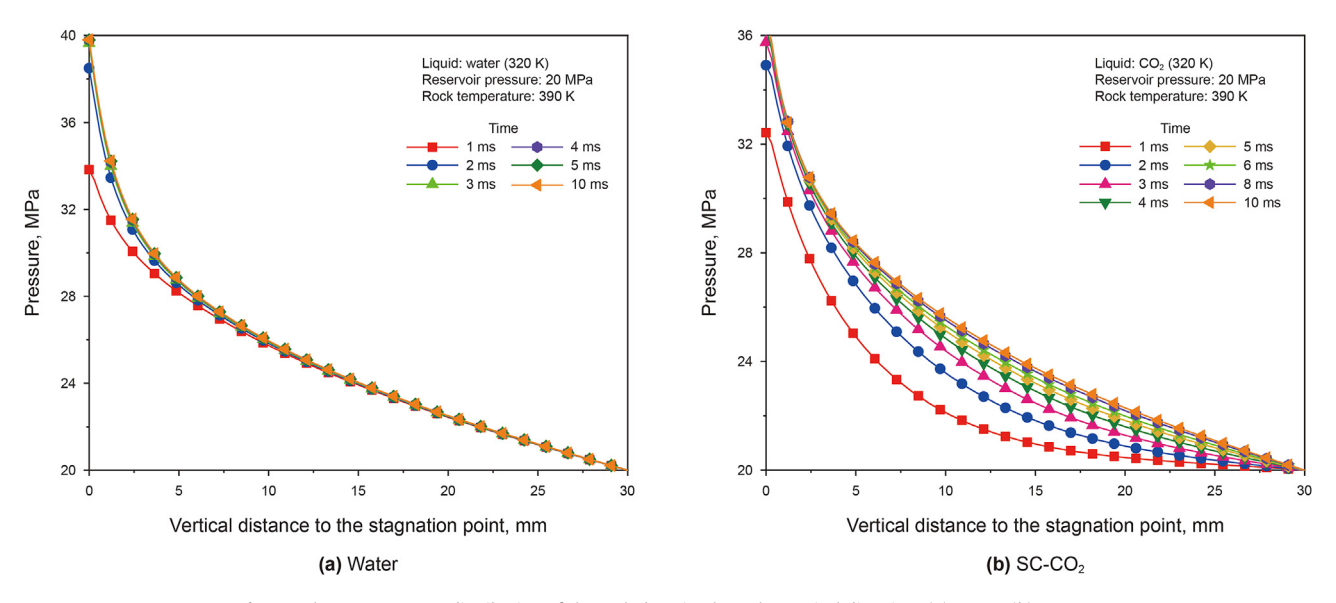


Fig. 21. The pore pressure distribution of the rock domain along the vertical direction: (a) water; (b) SC-CO<sub>2</sub>.

about four times simultaneously. The reason is that as the temperature increases, the density and viscosity of SC-CO<sub>2</sub> will decrease simultaneously. That leads to the high jet velocity and high particle velocity. However, low viscosity means a low drag force. Therefore, it can be seen that the gap between the jet velocity and particle velocity gradually becomes larger. A suitable temperature increase on the ground could improve the SC-CO<sub>2</sub> jet perforation effect in field applications.

# 4.2. Carbonate rock stress field

# 4.2.1. Maximum principle stress

Based on the first strength theory, brittleness material fails when the max principal stresses exceed its tensile strength. Therefore, by studying the max principal stress distribution, we could figure out the tensile failure pattern of carbonate rock under jet impingement. Generally, the tensile stress is set as positive, while the compressive stress is set as negative. Fig. 14 shows the

contours of maximum principle stress subjected to water and  $SC-CO_2$  jet impingement. Carbonate rock showed a similar failure pattern under different jet mediums. The compressive stress was mainly distributed at the center of the surface. In comparison, the tensile stress was distributed with a ring pattern and gradually enhanced along the radial direction.

We extracted the stress distribution along radial and vertical directions to better represent the failure pattern. In Fig. 15, the change of the maximum principle stress of two jets showed a similar evolution process. The compressive stresses at the stagnation point increased slightly in the initial few milliseconds on both conditions. With the increase in the radial distance, the stress value switched from negative to positive at about 12.5 mm. The tensile stress increased significantly at the boundary of the jet hole. It is mainly attributed to the stress concentration at the edge of the jet hole. The differences between the two jets were the stress value at the stagnation point and the edge of the jet hole. The carbonate rock suffered higher compressive stress under the water jet and a

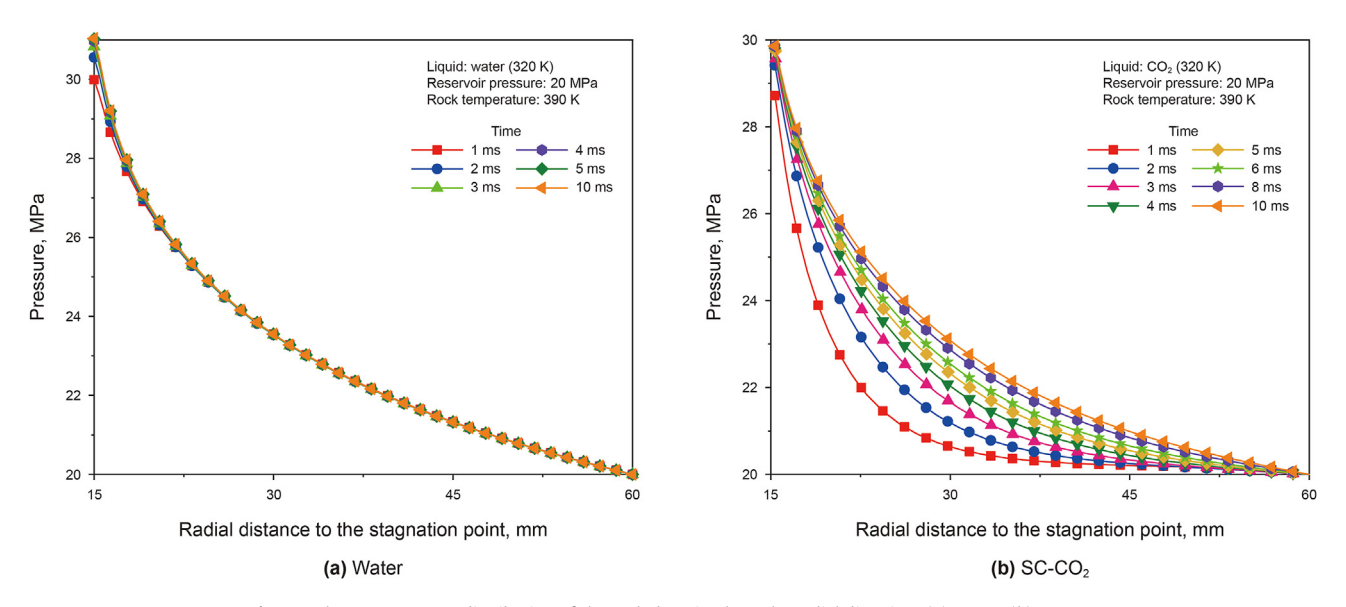


Fig. 22. The pore pressure distribution of the rock domain along the radial direction: (a) water; (b) SC-CO<sub>2</sub>.

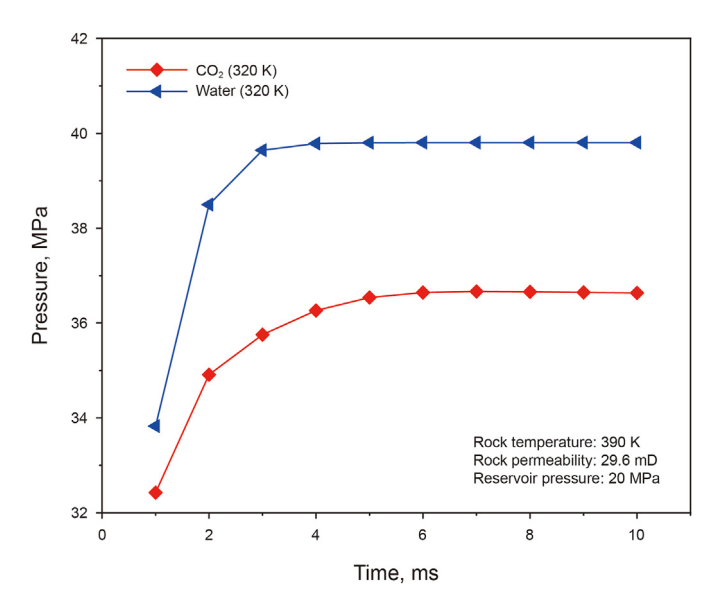


Fig. 23. The pressure distribution at the stagnation point of water and SC-CO<sub>2</sub>.

much higher tensile stress under the SC-CO<sub>2</sub> jet. It is consistent with the previous discussion (Fig. 11) that SC-CO<sub>2</sub> jet velocity dissipated more significantly when the jet reached the bottom rock surface. This process also involved the phase change and the volume expansion of CO<sub>2</sub>. Therefore, it led to lower impingement stress at the stagnation point and higher tensile stress at the jethole surface. Fig. 16 presents the maximum principle stress distribution along the vertical line of the water jet and SC-CO<sub>2</sub> jet, respectively. It can be seen that both stress curves went through the same changing process. In the initial few milliseconds, the compressive stress at the stagnation point increased with time. At about 6 ms, the stress reached stable. The compressive stress switched to tensile stress at about 10 mm below the stagnation point.

#### 4.2.2. Mises stress

Von Mises stress is a yield criterion that follows the fourth strength theory. It is defined by the equation as follows:

$$\sigma_{e} = \sqrt{\frac{(\sigma_{1} - \sigma_{2})^{2} + (\sigma_{2} - \sigma_{3})^{2} + (\sigma_{3} - \sigma_{1})^{2}}{2}}$$
(16)

where  $\sigma_e$  is the equivalent stress;  $\sigma_1$ ,  $\sigma_2$  and  $\sigma_3$  are the first, second, and third principal stress, respectively.

According to the distribution of Mises stress, we can figure out the area likely to fail during the jet fracturing process. Fig. 17 shows the Mises stress contours of carbonate rock under water jet and SC-CO<sub>2</sub> jet impingement. It can be seen that the distribution of both mises stress contours originated from the jet-hole and extended to the rock boundary. We extracted the Mises stress distribution along the radial and vertical directions. As shown in Fig. 18, the value of Mises stress decreased first with the increase in the radial distance. It then increased, forming the circular ring pattern. This changing pattern of Mises stress on the impact surface was helpful for rock failure. The obstruction of the perforation edge changed the trend of Mises stress. The changing Mises stress showed the same distribution features as the maximum principle stress. The carbonate rock takes a higher Mises stress at the stagnation point under the water jet. While in the SC-CO<sub>2</sub> jet, the Mises stress at the jet-hole surface was much higher. Fig. 19 shows the Mises stress along the vertical direction. It can be seen that the maximum Mises stress in rock was located below the stagnation point at about 5 mm. And the stress value under the SC-CO<sub>2</sub> jet was higher than the water jet at this point. The shear failure was more likely to occur in this area

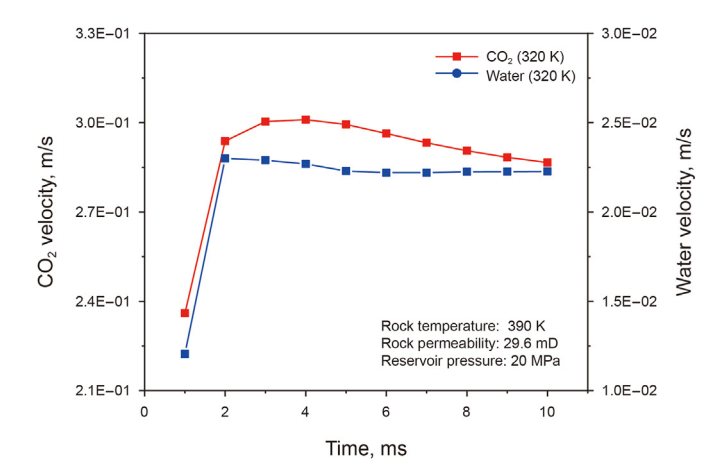


Fig. 25. The seepage velocity distribution of water and SC-CO<sub>2</sub> at the stagnation point.

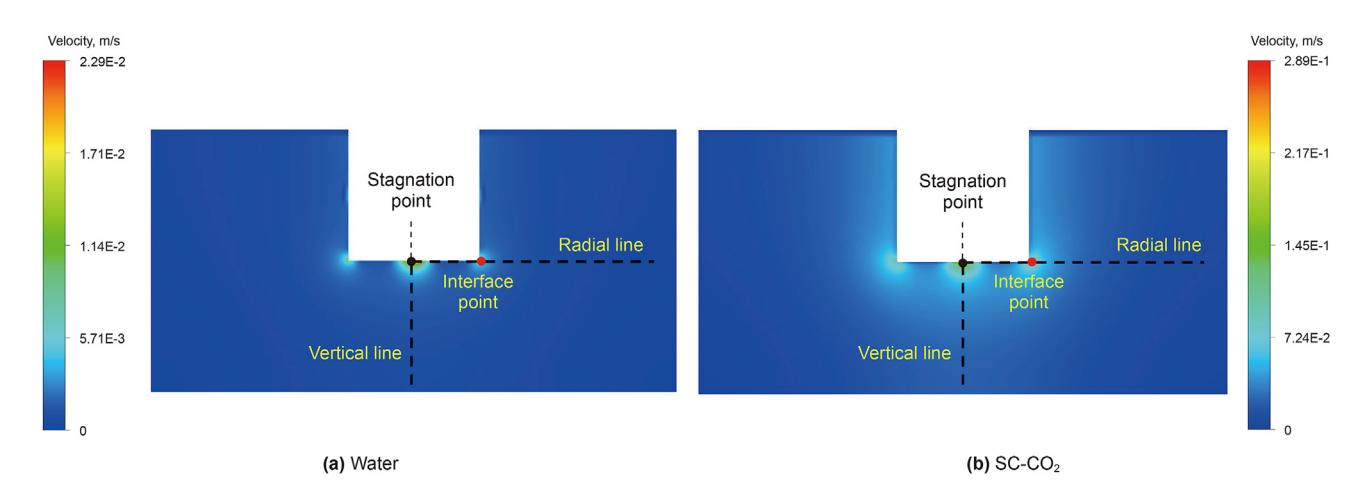


Fig. 24. The seepage velocity contours of (a) water and (b) SC-CO<sub>2</sub>.

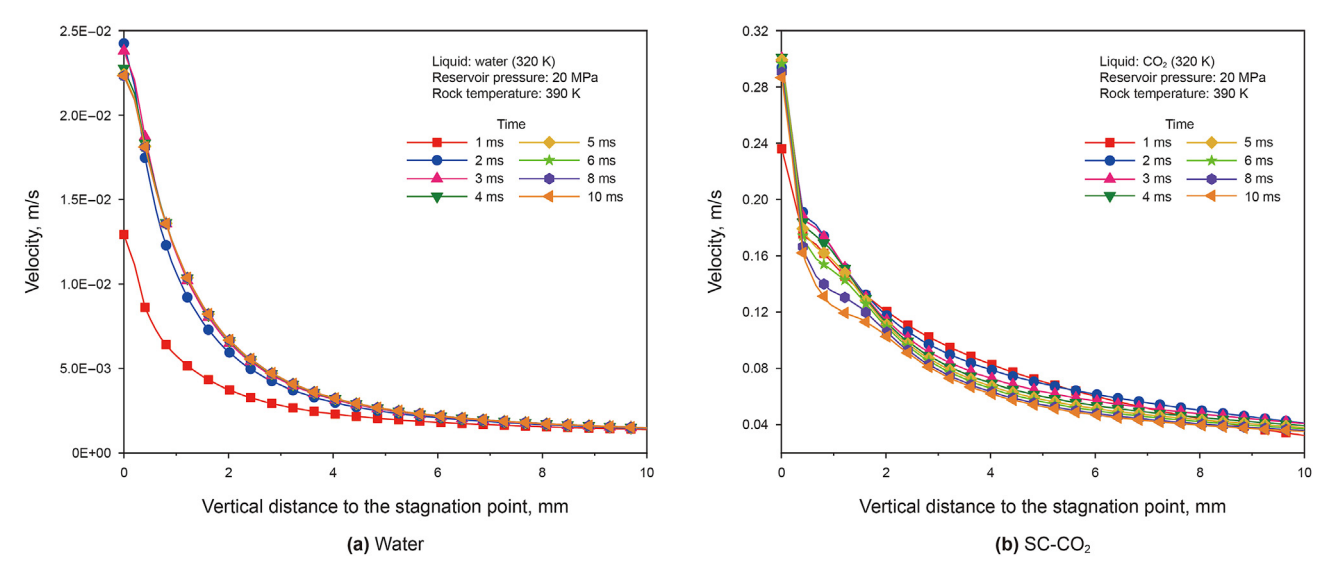


Fig. 26. The seeping velocity distribution of rock domain along the vertical direction: (a) water; (b) SC-CO<sub>2</sub>.

during high  $SC-CO_2$  jets. The fracture initiation and propagation would start from this failure point to the weak point on the impact surface.

# 4.3. Porous flow field

#### 4.3.1. Pressure distribution of porous flow field

Fig. 20 illustrates the pressure distribution of rock under jet impingement. It can be seen that from the jet-hole to the rock boundary, the pressure dropped gradually. Moreover, according to Figs. 21 and 22, water pressure reached stabilization faster than SC-CO<sub>2</sub> in both directions (vertical and radial). It is mainly related to the low viscosity and the compressibility of SC-CO<sub>2</sub>. The low viscosity and near-zero surface tension made transporting into the porous domain easier. This seeping mechanism could increase the pore pressure around the wellbore and reduce the strength of the rock. However, the compressible characteristic slowed down the speed of pressure propagation. The previous experiments also presented the phenomenon that the wellbore bottom pressure of

 $SC-CO_2$  increases more slowly than water during the fracturing (lian et al., 2021).

Moreover, this unique property also lowered the stagnation point pressure (Fig. 23). At the stagnation point, the pressure of the water jet is 4 MPa higher than the SC-CO<sub>2</sub> jet. The SC-CO<sub>2</sub> might need a higher pump pressure for the same crack extension effect. However, the carbonate geothermal reservoir could avoid this problem due to the chemical reaction between CO<sub>2</sub> and water formation. After CO<sub>2</sub> was injected into the pore structure, it could combine with water and produce carbonic acid. The release of H<sup>+</sup> leads to mineral dissolution (Cui et al., 2017). Mineral and clay dissolution helps create microfractures, improving the fracturing effect. And the high reservoir temperature could accelerate this process. Therefore, the carbonate geothermal reservoir is one of the best formations for SC-CO<sub>2</sub> jet fracturing.

# 4.3.2. Velocity distribution of porous flow field

Fig. 24 shows the seepage velocity contours in the rock domain of water and  $SC-CO_2$ , respectively. To describe the velocity

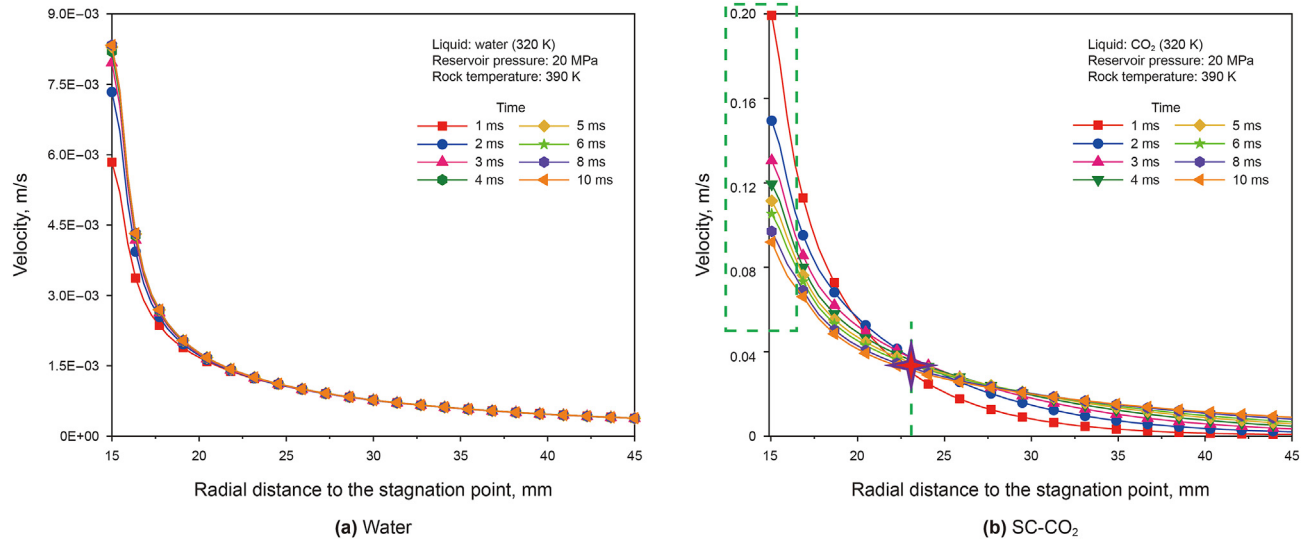


Fig. 27. The seeping velocity distribution of rock domain along the radial direction: (a) water; (b) SC-CO<sub>2</sub>.

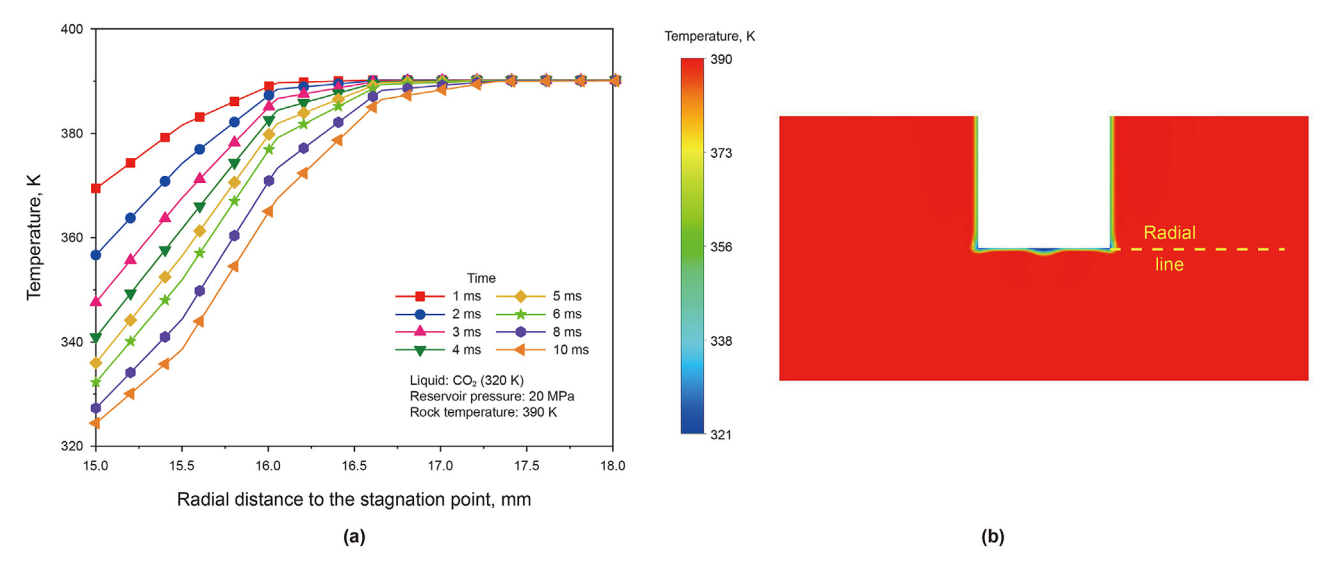


Fig. 28. The temperature distribution of the rock domain along the radial direction.

distribution clearly, we marked two points and two direction lines in Fig. 24 (stagnation point, interface point, vertical line and radial line). It can be seen that the high seeping velocity area was located at the nearby stagnation point and interface point. As illustrated in Fig. 25, the seeping velocity of SC-CO<sub>2</sub> was about 13 times that of water. The distribution on vertical and radial lines showed similar results with the stagnation point. The velocity of SC-CO<sub>2</sub> was much higher than water in both directions. And then, they all gradually decreased to stabilization from a high value (Fig. 26). The distribution character of higher seeping velocity had the same mechanism as the pore pressure mentioned above. It is attributed to the low viscosity and near-zero surface tension of SC-CO<sub>2</sub>. The SC-CO<sub>2</sub> can easily seep into the pore structure and help create microfractures.

However, the seeping velocity of SC-CO<sub>2</sub> in the radial direction presented a different changing process. At the vicinity interface point (Fig. 27), the seeping velocity gradually decreased from 0.199 to 0.091 m/s with time. However, when the distance exceeded 23 mm, the seeping velocity gradually increased with time.

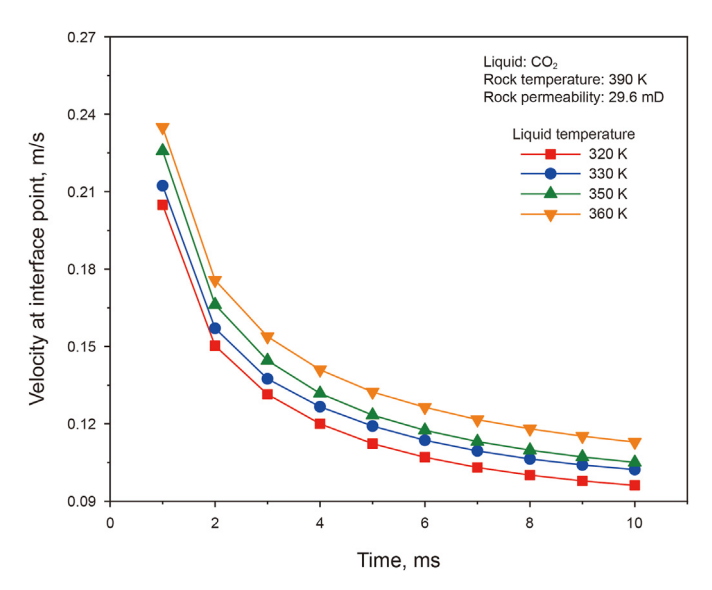


Fig. 29. The velocity at interface point with different temperatures.

This unique phenomenon is attributed to the seeping process of SC-CO<sub>2</sub> being controlled by pressure and temperature simultaneously. Fig. 28a shows the temperature distribution curve along the radial direction. We found that the temperature decreased (from 369 to 324 K) at the nearby interface point as time passed. This change occurs because, under the continual jet impingement, the rock (390 K) was gradually cooled down by the fluid (320 K). As illustrated in the previous section, the rheological of SC-CO<sub>2</sub> was affected by the temperature significantly. The high temperature could decrease the density and viscosity of SC-CO<sub>2</sub>, which led to the high seeping velocity. Therefore, the change in seeping velocity of SC-CO<sub>2</sub> along the radial direction shows the different patterns in Fig. 27.

The increase of seeping velocity in the later stage can be attributed to the limited speed of heat conduction. Fig. 28a shows that the temperature remains unchanged when the distance exceeds 17 mm. The main controlling factor of seeping velocity began to switch from temperature to pressure in this region. The pore pressure increased gradually with time passing by in this region (Fig. 22). The high pressure provided high kinetic energy. It explained the change of the seeping velocity curve when the distance was above 23 mm. This phenomenon also can be verified in Fig. 29. When we increased the jet flow temperature, the seeping velocity at the interface point also augmented simultaneously. Therefore, increasing fluid temperature in the ground could promote the seepage process and help create microfractures in applications.

#### 5. Conclusions

This study explored the feasibility of using SC-CO<sub>2</sub> jet fracturing, an environmentally benign fluid, to stimulate the carbonate geotherm reservoirs. The purpose of this technology was to improve the connectivity of fracture networks and realize the storage of CO<sub>2</sub> simultaneously. To evaluate the performance of this method, we built a transient fluid-thermo-mechanical coupled model to analyze the flow field of SC-CO<sub>2</sub> jet fracturing. Moreover, we considered the physical properties change of SC-CO<sub>2</sub> with temperature simultaneously in the model. Through analysis of this simulation, the main conclusions were drawn as follows:

- (1) Due to the low viscosity and density of SC-CO<sub>2</sub>, the maximum jet velocity and particle velocity of the SC-CO<sub>2</sub> jet are 2.08% and 1.59% higher than that of the water jet, respectively. Therefore, SC-CO<sub>2</sub> will perform better in jet perforation under the same boundary conditions. In addition, increasing jet temperature could improve the jet and particle velocity effectively.
- (2) The maximum particle erosion rate of the SC-CO<sub>2</sub> jet is about four times that of the water jet. The erosion contour under water jet presented a ring shape, while that of the SC-CO<sub>2</sub> presented a more centralized circle. The centralized erosion pattern is in favor of increasing the perforation efficiency. Therefore, SC-CO<sub>2</sub> jet perforation could achieve the same perforation effect as the water jet in a lower particle density. Simultaneously, this could reduce the risk of sand plugging.
- (3) Carbonate rock stress distribution showed that the tensile and shear failure would more easily occur under the SC-CO<sub>2</sub> jet than the water jet. And the max principal stress and the Mises stress reached the peak value at the edge of the jet hole.
- (4) Compared with the water jet, SC-CO<sub>2</sub> can seep into the pore structure more easily. Both pressure and temperature control the seepage of SC-CO<sub>2</sub> in the geothermal reservoir. Furthermore, the temperature was the main controlling factor near the jet-hole wall. The higher fluid temperature could promote seepage by changing the rheological properties of the SC-CO<sub>2</sub>.

#### Acknowledgment

The authors would like to acknowledge the National Key R&D Program of China (No. 2019YFB1504102).

#### References

- Ameri, A., Sodeifian, G., Sajadian, S.A., 2020. Lansoprazole loading of polymers by supercritical carbon dioxide impregnation: impacts of process parameters. J. Supercrit, Fluids 164, 104892. https://doi.org/10.1016/j.supflu.2020.104892.
- Ardestani, N.S., Sodeifian, G., Sajadian, S.A., 2020. Preparation of phthalocyanine green nano pigment using supercritical CO<sub>2</sub> gas antisolvent (GAS): experimental and modeling. Heliyon 6 (9), e04947. https://doi.org/10.1016/j.heliyon.2020.e04947.
- Bennon, W.D., Incropera, F.P., 1987. A continuum model for momentum, heat and species transport in binary solid-liquid phase change systems—I. Model formulation. Int. J. Heat Mass Tran. 30 (10), 2161–2170. https://doi.org/10.1016/ 0017-9310(87)90094-9.
- Cai, C., Wang, X., Mao, S., et al., 2017. Heat transfer characteristics and prediction model of supercritical carbon dioxide (SC-CO<sub>2</sub>) in a vertical tube. Energies 10 (11), 1870. https://doi.org/10.3390/en10111870.
- Cai, C., Kang, Y., Wang, X., et al., 2018. Mechanism of supercritical carbon dioxide (SC-CO<sub>2</sub>) hydro-jet fracturing. J. CO<sub>2</sub> Util. 26, 575–587. https://doi.org/10.1016/ j.jcou.2018.06.012.
- Cai, C., Kang, Y., Yang, Y., et al., 2020. Experimental investigation on flow field and induced strain response during SC-CO<sub>2</sub> jet fracturing. J. Petrol. Sci. 195, 107795. https://doi.org/10.1016/j.petrol.2020.107795.
- Cai, C., Li, B.R., Zhang, Y.Y., et al., 2022. Fracture propagation and induced strain response during supercritical CO<sub>2</sub> jet fracturing. Petrol. Sci. https://doi.org/10.1016/j.petsci.2022.03.019.
- Chang, P., Xu, G., Zhou, F., et al., 2019. Comparison of underground mine DPM simulation using discrete phase and continuous phase models. Process Saf. Environ. Protect. 127, 45–55. https://doi.org/10.1016/j.psep.2019.04.027.
- Chen, Y., Ma, G., Wang, H., et al., 2019. Application of carbon dioxide as working fluid in geothermal development considering a complex fractured system. Energy 180, 1055–1067. https://doi.org/10.1016/j.enconman.2018.11.046.
- Cui, G., Zhang, L., Ren, B., et al., 2016. Geothermal exploitation from depleted high temperature gas reservoirs via recycling supercritical CO<sub>2</sub>: heat mining rate and salt precipitation effects. Appl. Energy 183, 837–852. https://doi.org/10.1016/ j.apenergy.2016.09.029.
- Cui, G., Zhang, L., Tan, C., et al., 2017. Injection of supercritical CO<sub>2</sub> for geothermal exploitation from sandstone and carbonate reservoirs: CO<sub>2</sub>—water—rock interactions and their effects. J. CO<sub>2</sub> Util. 20, 113–128. https://doi.org/10.1016/j.jcou.2017.05.006.
- Edwards, J., McLaury, B., Shirazi, S., 2000. Evaluation of alternative pipe bend fittings in erosive service. In: 2000 ASME Fluids Engineering Division Summer

#### Meeting.

- Fenghour, A., Wakeham, W.A., Vesovic, V., 1998. The viscosity of carbon dioxide. J. Phys. Chem. Ref. Data 27 (1), 31–44. https://doi.org/10.1063/1.556013.
- He, Z., Tian, S., Li, G., et al., 2015. The pressurization effect of jet fracturing using supercritical carbon dioxide. J. Nat. Gas Sci. 27, 842–851. https://doi.org/ 10.1016/j.jngse.2015.09.045.
- Homuth, S., Götz, A.E., Sass, I., 2015. Physical properties of the geothermal carbonate reservoirs of the Molasse Basin, Germany—outcrop analogue vs. reservoir data. World Geothermal Congress 19–24.
- Hu, Y., Kang, Y., Wang, X., et al., 2016. Experimental and theoretical analysis of a supercritical carbon dioxide jet on wellbore temperature and pressure. J. Nat. Gas Sci. Eng. 36, 108–116. https://doi.org/10.1016/j.jngse.2016.10.014.
- Hu, Y., Liu, Y., Cai, C., et al., 2017. Fracture initiation of an inhomogeneous shale rock under a pressurized supercritical CO<sub>2</sub> jet. Appl. Sci. 7 (10), 1093. https://doi.org/ 10.3390/app7101093.
- Huang, M., Kang, Y., Wang, X., et al., 2018. Experimental investigation on the impingement characteristics of a self-excited oscillation pulsed supercritical carbon dioxide jet. Exp. Therm. Fluid Sci. 94, 304–315. https://doi.org/10.1016/ j.expthermflusci.2018.02.015.
- Jian, G., Li, Z., Bo, G., et al., 2021. Formation of fractures in carbonate rocks by pad acid fracturing with different states of carbon dioxide. Petrol. Explor. Dev. 48 (3), 744-751, https://doi.org/10.1016/S1876-3804(21)60060-5.
- Li, C., Wu, Y., Wang, Y., et al., 2020. Analysis on the behavior of dispersed plate-type fuel based on fluid-solid coupling method. Prog. Nucl. Energy 126, 103398. https://doi.org/10.1016/j.pnucene.2020.103398.
- Li, G., Huang, Z., Tian, S., et al., 2010. Research and application of water jet technology in well completion and stimulation in China. Petrol. Sci. 7 (2), 239–244. https://doi.org/10.1007/s12182-010-0009-9.
- Niederau, J., Ebigbo, A., Marquart, G., et al., 2015. Assessment and simulation of various utilization scenarios of a medium-enthalpy reservoir in southern Italy (Guardia Lombardi). Assessment 19, 25.
- Razmimanesh, F., Sodeifian, G., Sajadian, S.A., 2021. An investigation into Sunitinib malate nanoparticle production by US-RESOLV method: effect of type of polymer on dissolution rate and particle size distribution. J. Supercrit. Fluids 170, 105163. https://doi.org/10.1016/j.supflu.2021.105163.
- Sodeifian, G., Ardestani, N.S., Sajadian, S.A., et al., 2016a. Application of supercritical carbon dioxide to extract essential oil from Cleome coluteoides Boiss: experimental, response surface and grey wolf optimization methodology. J. Supercrit. Fluids 114, 55–63. https://doi.org/10.1016/j.supflu.2016.04.006.
- Sodeifian, G., Sajadian, S.A., Ardestani, N.S., 2016b. Optimization of essential oil extraction from Launaea acanthodes Boiss: utilization of supercritical carbon dioxide and cosolvent. J. Supercrit. Fluids 116, 46–56. https://doi.org/10.1016/ i.supflu.2016.05.015.
- Sodeifian, G., Sajadian, S.A., Ardestani, N.S., 2017. Determination of solubility of Aprepitant (an antiemetic drug for chemotherapy) in supercritical carbon dioxide: empirical and thermodynamic models. J. Supercrit. Fluids 128, 102–111. https://doi.org/10.1016/j.supflu.2017.05.019.
- Sodeifian, G., Razmimanesh, F., Sajadian, S.A., 2019a. Solubility measurement of a chemotherapeutic agent (Imatinib mesylate) in supercritical carbon dioxide: assessment of new empirical model. J. Supercrit. Fluids 146, 89–99. https:// doi.org/10.1016/j.supflu.2019.01.006.
- Sodeifian, G., Ardestani, N.S., Sajadian, S.A., et al., 2019b. Experimental measurements and thermodynamic modeling of Coumarin-7 solid solubility in supercritical carbon dioxide: production of nanoparticles via RESS method. Fluid Phase Equil. 483, 122–143. https://doi.org/10.1016/j.fluid.2018.11.006.
- Sodeifian, G., Sajadian, S.A., Derakhsheshpour, R., 2020a. Experimental measurement and thermodynamic modeling of Lansoprazole solubility in supercritical carbon dioxide: application of SAFT-VR EoS. Fluid Phase Equil. 507, 112422. https://doi.org/10.1016/j.fluid.2019.112422.
- Sodeifian, G., Garlapati, C., Hazaveie, S.M., et al., 2020b. Solubility of 2,4,7-triamino-6-phenylpteridine (triamterene, diuretic drug) in supercritical carbon dioxide: experimental data and modeling. J. Chem. Eng. Data 65 (9), 4406–4416. https://doi.org/10.1021/acs.jced.0c00268.
- Sodeifian, G., Garlapati, C., Razmimanesh, F., et al., 2021. The solubility of Sulfabenzamide (an antibacterial drug) in supercritical carbon dioxide: evaluation of a new thermodynamic model. J. Mol. Liq. 335, 116446. https://doi.org/10.1016/j.molliq.2021.116446.
- Sheng, M., Li, G., Huang, Z., et al., 2013. Experimental study on hydraulic isolation mechanism during hydra-jet fracturing. Exp. Therm. Fluid Sci. 44, 722–726. https://doi.org/10.1016/j.expthermflusci.2012.09.014.
- Shi, Y., Song, X., Wang, G., et al., 2019. Study on wellbore fluid flow and heat transfer of a multilateral-well CO<sub>2</sub> enhanced geothermal system. Appl. Energy 249, 14–27. https://doi.org/10.1016/j.apenergy.2019.04.117.
- Span, R., 2013. Multiparameter Equations of State: an Accurate Source of Thermodynamic Property Data. Springer Science & Business Media.
- Span, R., Wagner, W.J., 1996. A new equation of state for carbon dioxide covering the fluid region from the triple-point temperature to 1100 K at pressures up to 800 MPa. J. Phys. Chem. Ref. Data 25 (6), 1509–1596. https://doi.org/10.1063/ 1.555991.
- Tummers, M.J., Jacobse, J., Voorbrood, S.G., et al., 2011. Turbulent flow in the near field of a round impinging jet. Int. J. Heat 54 (23–24), 4939–4948. https://doi.org/10.1016/j.ijheatmasstransfer.2011.07.007.
- Vafai, K., Tien, C.L., 1981. Boundary and inertia effects on flow and heat transfer in porous media. Int. J. Heat Mass Tran. 24 (2), 195–203. https://doi.org/10.1016/0017-9310(81)90027-2.

- Versteeg, H.K., Malalasekera, W., 2007. An Introduction to Computational Fluid Dynamics: the Finite Volume Method, Pearson Education.
- Wang, H.-Z., Li, G.-S., Tian, S.-C., et al., 2015. Flow field simulation of supercritical carbon dioxide jet: comparison and sensitivity analysis. J. Hydrodyn. 27 (2), 210–215. https://doi.org/10.1016/S1001-6058(15)60474-7.
- Wang, H., Yu, Y., Yu, J., et al., 2019. Numerical simulation of the erosion of pipe bends considering fluid-induced stress and surface scar evolution. Wear 440, 203043. https://doi.org/10.1016/j.wear.2019.203043.
- Wang, Z., Zhang, C., Jiang, G., et al., 2021. Effect of different exploitation schemes on production performance from the carbonate reservoir: a case study in Xiong'an new area. J. Clean. Prod. 314, 128050. https://doi.org/10.1016/j.jclepro.2021.128050.
- Wu, S., Ge, H., Li, T., et al., 2022. Characteristics of fractures stimulated by supercritical carbon dioxide fracturing in shale based on acoustic emission monitoring. Int. J. Rock Mech. Min. Sci. 152, 105065. https://doi.org/10.1016/ j.ijrmms.2022.105065.
- Wu, X., Huang, Z., Zhao, H., et al., 2019. A transient fluid-thermo-structural coupling study of high-velocity LN2 jet impingement on rocks. Int. J. Rock Mech. Min. Sci. 123, 104061. https://doi.org/10.1016/j.ijrmms.2019.104061.
- Xu, H., Cheng, J., Zhao, Z., 2020. Numerical study and application of acid-fracturing in the carbonate geothermal reservoirs from North China. Acta Geol. Sin. 94 (7), 2157–2165. https://doi.org/10.3724/SP.I.0001-571720200724.
- Zhai, K., Fang, H., Guo, C., et al., 2021. Mechanical properties of CFRP-strengthened prestressed concrete cylinder pipe based on multi-field coupling. Thin-Walled Struct. 162, 107629. https://doi.org/10.1016/j.tws.2021.107629.
- Zhang, S., Huang, Z., Huang, P., et al., 2018a. Numerical and experimental analysis of hot dry rock fracturing stimulation with high-pressure abrasive liquid nitrogen jet. J. Petrol. Sci. Eng. 163, 156–165. https://doi.org/10.1016/j.petrol.2017.12.068.
- Zhang, S., Huang, Z., Wang, H., et al., 2018b. Thermal characteristics analysis with local thermal non-equilibrium model during liquid nitrogen jet fracturing for HDR reservoirs. Appl. Therm. Eng. 143, 482–492. https://doi.org/10.1016/j.applthermaleng.2018.07.088.